Classification of Post Synaptic Current Events Recorded from a Dissociated Purkinje Cell Soma and the Role Presynaptic Receptors

CoMPLEX MRes summer project at UCL

Peter Hebden

August 2019

Contents

Abbreviations

AIS	axon initial segment
AMPA	α-amino-3-hydroxy-5-methyl-4-isoxazolepropionic acid
AMPAR	AMPA receptor
ANN	artificial neural network
B1	data file bicc-1 or "16630001.abf"
B2	data file bicc-2 or "16728001 v3.abf"
B3	data file bicc-3 or "16728003.abf"
B4	data file bicc-4 or "16922000.abf"
bicc	bicuculline
BC	basket cell
D1	data file DNQX-1 or "09n17004 v2.abf"
D2	data file DNQX-2 or "09921004.abf"
D3	data file DNQX-3 or "16405000.abf"
D4	data file DNQX-4 or "16525000.abf"
D5	data file DNQX-5 or "16526000.abf"
D6	data file DNQX-6 or "16513000.abf"
DNQX	6,7-dinitroquinoxaline-2, 3-dione
DPE	depolarization-induced suppression of excitation
DPI	depolarization-induced suppression of inhibition
EPSC	excitatory postsynaptic current
FN	false negative
FNR	false negative rate
FP	false positive
FPR	false positive rate
GABA	gamma-aminobutyric acid
GABAR	GABA receptor
GC	granule cell
GT	ground truth
IPSC	inhibitory postsynaptic current
LC	Lugaro cell
MLI	molecular layer interneurons
N1	data file NMDA-1 or "08603001.abf"
NMDA	N-methyl-D-aspartate
NMDAR	NMDA receptor
NN	neural network
PF	parallel fibre
PSP	postsynaptic potential
PC	Purkinje cell
PMCA	plasma membrane Ca^{2+}-ATPase
preNMDAR	presynaptic NMDA receptor
SC	stellate cell
SERCA	sarco/endoplasmic reticulum Ca^{2+}-ATPase
ssGlyR	strychnine-sensitive glycine receptor
TP	true positive
TPR	true positive rate
TN	true negative
TNR	true negative rate
UBC	unipolar brush cell
VGCC	voltage gated calcium channel

Abstract

The recording and analysis of synaptic currents can provide an informative measure of neuronal and circuit behaviour, but recordings from the soma of dissociated Purkinje cells contain an overlapping mixture of slow (gabaergic) and fast (glutamatergic) events with highly variable kinetics. These events trigger complex synaptic feedback interactions with the presynaptic terminals under physiological conditions that are lost when events of one type are blocked.

The aim of this report is to investigate whether or not neural networks provide a practical method for the classification of events recorded before the application of blockers. My results indicate that while traditional template based methods are somewhat effective, a neural network based method can be more accurate, more reliable, easier to apply, and may provide better information about synaptic interactions and the role of presynaptic receptors.

1 Introduction

The recording and analysis of synaptic currents is one of the most useful and informative measures of cell and circuit behaviour in neuroscience. Many methods of analysis have been developed [4, 21, 28, 29, 30, 49, 67, 76, 81, 83, 94]. Although these methods can be effective for some applications, in general, they are not well suited to the detection and classification of overlapping events with highly variable kinetics.

Artificial neural networks (ANNs) are class of machine learning methods. They are flexible and can accurately model relatively small irregularities in functions. Even a network with a single hidden layer can model any continuous function if the hidden layer contains enough nodes (artificial neurons) [47]. They are a promising alternative to traditional template methods of event detection and classification.

Multiple event types are common and can arise in a number of ways. Excitatory synaptic currents with or without an N-methyl-D-aspartate (NMDA) receptor component have distinct kinetic behaviours. Excitatory and inhibitory synaptic currents also have distinct kinetics. Event overlap in terms of time and kinetics obscures detection and classification. Consequently, experimenters have often simplified their analysis by blocking either excitatory or inhibitory receptors, but receptor blocking interferes with normal interactions and the study of presynaptic regulation. For example, do presynaptic glycine receptors on the climbing fibre (CF) boutons regulate glutamate release [5, 55], or do presynaptic NMDA receptors on interneurons regulate γ-aminobutyric acid (GABA) release?

Presynaptic receptors are ideally located to influence neurotransmitter release [59], and retrograde signalling provides an efficient feedback mechanism that enables postsynaptic neurons to control their presynaptic inputs [35]. This report is focussed on the synaptic interactions at a single Purkinje cell where presynaptic NMDA receptors on basket cell terminals receive a retrograde signal from the post synaptic Purkinje cell; they mediate positive feedback from the Purkinje cell in a way that facilitates the release of GABA from the basket cell and, in turn, increases inhibition of the Purkinje cell [41].

Synaptic interactions at Purkinje cells are complex. In addition to AMPA and $GABA_A$ postsynaptic receptors on the Purkinje cell, there are presynaptic receptors on the climbing

fibre and the Basket cells. The potential impact of presynaptic receptors is an important consideration.

The first aim of this project is to examine methods of event detection and classification for whole cell voltage clamp recordings that include a mixture of post synaptic current (PSC) events with highly variable amplitudes and kinetics that may overlap in time. The second aim is to elucidate the existence and role presynaptic receptors at the basket cell–Purkinje cell synapse.

2 Background

2.1 Purkinje cells

Purkinje cells are a class of GABAergic neurons in the cerebellum. Figure 1 shows a schematic of the excitatory and inhibitory inputs to a Purkinje cell. It receives excitatory inputs from parallel fibres (PFs) and climbing fibres (CFs) [40].

The PFs make about 200,000 relatively weak excitatory (glutamatergic) synapses onto spines in the Purkinje cell's dendrite [100]. Climbing fibres originating from the inferior olivary nucleus provide powerful excitatory input to the Purkinje cell's proximal dendrites and soma. One climbing fibre contacts one to ten Purkinje cells [37]. Each Purkinje cell receives input from one climbing fibre with about 500 synapses [80, 104].

The basket cells (BCs) and stellate cells (SCs) in this report are interneurons in the molecular layer of the cerebellum. Both provide inhibitory (GABAergic) input to the Purkinje cell, with basket cells synapsing mostly on the Purkinje cell soma and axon initial segment, and stellate cells on the dendrites [40, 80].

The stimulation of a small number of mossy fibres activates, via granule cells and their parallel fibres, an extensive array of Purkinje cells and all three types of inhibitory interneurons [38]. Consequently the activation of Purkinje cells by PFs is soon inhibited by BCs and SCs, which are activated by the same PFs. The net result is brief firing of a large sharply defined population of Purkinje cells [68].

Table 1 shows an overview of synapses and receptors, while Section 2.2 provides more details.

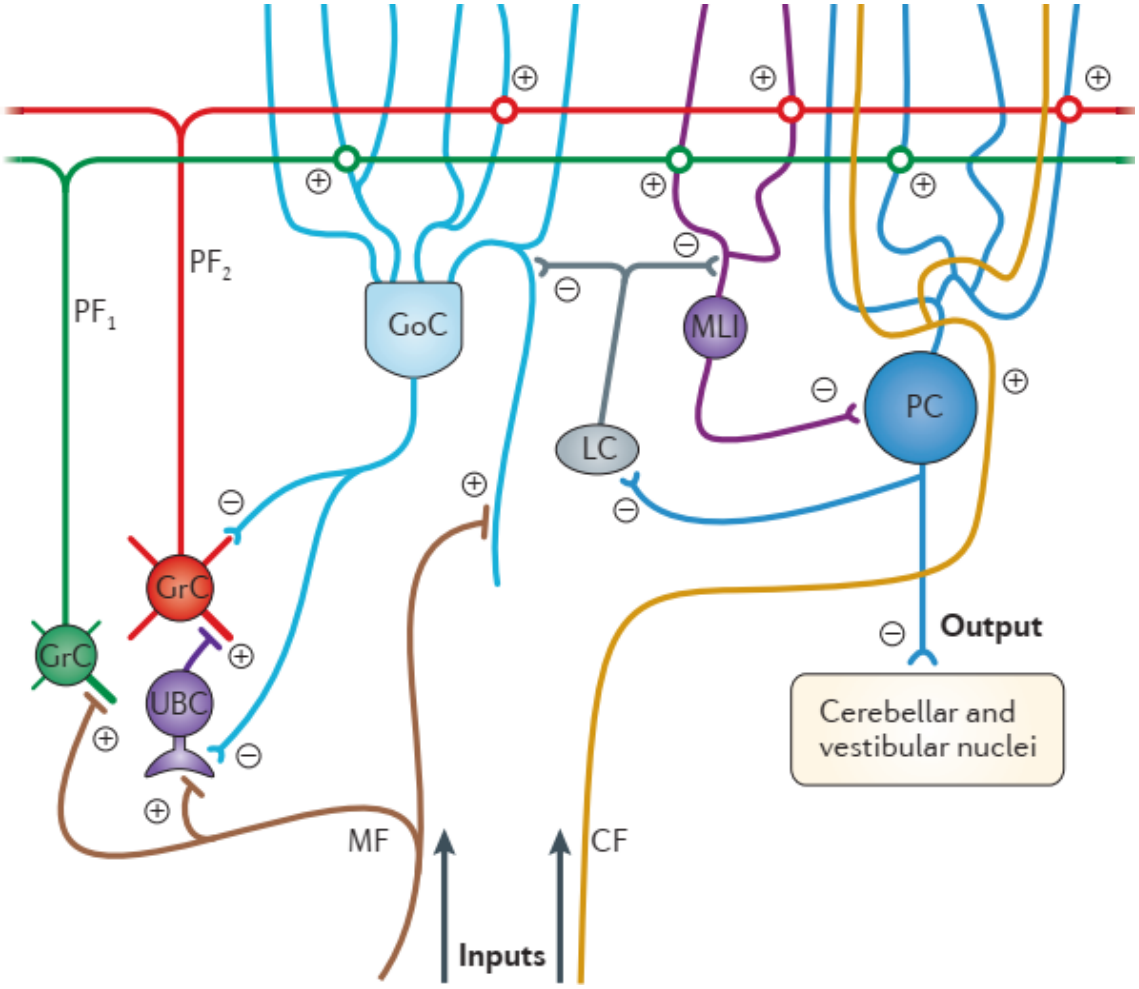

Figure 1: Purkinje cell synapses: Climbing fibres (CF) indirectly make excitatory synapses $\oplus$ with the PC's soma, while molecular layer interneurons (MLI), such as basket cells and stellate cells, make inhibitory synapses $\ominus$ with the PC's soma. Parallel fibres (PF) make excitatory synapses $\oplus$ with the PC's dendritic tree. Other components in this figure include mossy fibres (MF), unipolar brush cells (UBC), granule cells (GrC), Golgi cells (GoC), and the Lugaro cell (LC). Image from Box 1 "Layered character of the cerebellum and its position in the brain", part (b) in [40].

Synapse	Receptors		Postsynaptic Event	
	presynaptic	postsynaptic	EPSC	IPSC
PF–PC	NMDARs	AMPARs	fast	
CF–PC	NMDARs	AMPARs	fast	
BC–PC soma (AIS)	NMDARs	$GABA_A$		slow
SC–PC dendrites	NMDARs	$GABA_A$		slow

Table 1: Mature Purkinje cells receive excitatory input from PFs and CFs and inhibitory input from BCs and SCs [40]. Evidence from experiments suggests that presynaptic terminals have NMDA receptors (NMDARs). Basket cell (BC) terminals in particular are generally believed to have preNMDARs that mediate retrograde feedback from the postsynaptic cell, i.e. when the Purkinje cell releases glutamate, preNMDARs are well positioned to receive this signal and facilitate the release of GABA onto the Purkinje cell axon initial segment (AIS) [35]. In addition, climbing fibre (CF) terminals may also have glycine receptors [Personal communication: Professor Guy Moss, UCL].

2.2 Synapses and receptors

2.2.1 GABA and Glycine Receptors

Cells of the cerebellar nuclei have been broadly classified as excitatory (glutamatergic) and inhibitory (gabaergic). In mature animals, GABA and glycine are major inhibitory neurotransmitters because activated $GABA_A$ receptors and strychnine-sensitive glycine receptors allow the entry of Cl^- ions. However, they can act as excitatory neurotransmitters during early developmental periods when both GABA and glycine receptors allow the exit of Cl^- ions. The resulting depolarization occurs because of the relatively high intracellular Cl^- concentration [52].

The expression of functional glycine receptors has been found almost everywhere in the developing brain [5, 12, 108].

Classifications for local neurons and glycinergic neurons (that may provide feedback) have been proposed [101].

2.2.2 Postsynaptic NMDARs

Among principal neurons, adult Purkinje cells are well known for their lack of functional NMDA receptors. NMDA receptors are expressed in Purkinje cells of newborn animals, but lost after postnatal day (P)12 [75]. Accordingly, in juvenile and adult rats, CF stimulation gives rise to currents that are mediated predominantly by AMPA receptors on the Purkinje cell [88].

2.2.3 Presynaptic NMDARs

Presynaptic NMDARs enhance GABAergic transmission at cerebellar synapses from SC and BC molecular layer interneurons onto postsynaptic Purkinje cells [35, 41], but some results disagree [15, 84] as will be discussed in Section 5.3 of this report.

In rat cerebellar slices, activation of BC and SC presynaptic NMDA receptors triggers GABA release onto postsynaptic Purkinje cells in the presence of tetrodotoxin (TTX)

[41, 42]. The application of TTX prevented depolarisation via Na^+ channels (an action potential) which would cause Ca^{2+} influx via voltage gated calcium channels (VGCCs). However, Ca^{2+} influx via the preNMDARs could have depolarised the membrane and caused additional Ca^{2+} influx via VGCCs, and the resulting [Ca^{2+}] increase triggered the release of GABA [Personal communication: Professor Guy Moss, UCL].

NMDA induced a relatively large mIPSC frequency increase in basket and stellate cells, while mEPSCs were not affected [41], but the mechanism was not clear [42]. Intracellular Ca^{2+} stores can promote presynaptic neurotransmitter release [7, 17, 31]. Later research concluded that Ca^{2+} influx through the preNMDARs alone can be sufficient to drive presynaptic GABA release at the interneuron–Purkinje cell synapse in rat [42].

In this report, the preNMDARs on BC terminals that mediate retrograde signalling are of particular interest. They provide an efficient feedback mechanism that enables the PC to communicate with the BC and control transmitter release. Retrograde signalling is thought to operate at a variety of synapses throughout the brain [70]. However, while endocannabinoids, for example, operate almost everywhere throughout the brain, retrograde activation of presynaptic NMDARs appears to be confined to specific synapses in the cerebellum and hippocampus [34].

In general, retrograde mediated release requires stimulation of the postsynaptic cell, and the influx of Ca^{2+} [64, 109]. This results in a form of inhibitory synaptic plasticity known as depolarization-induced potentiation of inhibition (DPI) at interneuron–Purkinje cell synapses [35].

The presence of preNMDARs has been shown by many experiments. Figure 2(A) shows presynaptic autoreceptor activation in layer 5 (L5), (B) shows axo-axonic NMDAR activation, and (C) shows spillover-dependent NMDAR activation. However, Figure 2(D) is the most relevant to this report. It shows that Purkinje cell depolarisation together with Ca^{2+} influx was sufficient to ensure the activation of APV-sensitive NMDARs (APV is an NMDAR antagonist). The insensitivity of Purkinje cells to NMDA indicated that the locus of NMDAR expression must be presynaptic (at a glial cell or an interneuron) [35]. Following the activation of presynaptic NMDARs, Ca^{2+} influx via presynaptic NMDA channels, but not via voltage–gated Ca^{2+} channels, led to Ca^{2+} release from ryanodine-sensitive Ca^{2+} stores, and an increased release of GABA. The presence of functional presynaptic NMDARs was confirmed by patch clamp recording of single NMDA ion channel activity on basket and stellate cell terminals [35].

Definitive evidence of the source of glutamate release was provided by vibromechanically isolating Purkinje cells with attached GABA-releasing inhibitory axon terminals (nerve–bouton preparation [3, 103]). The ability to depolarise Purkinje cells and still activate presynaptic NMDARs proved that the retrograde glutamate was released from individual Purkinje cells [34].

However, results by Glitsch [42] showed that the NMDA-induced increase in presynaptic GABA release does not require activation of presynaptic VGCCs or Ca^{2+} release from presynaptic Ca^{2+} stores. Rather, Ca^{2+} influx through the NMDA receptor alone was sufficient to drive presynaptic GABA release at the rat interneuron–Purkinje cell synapse [42].

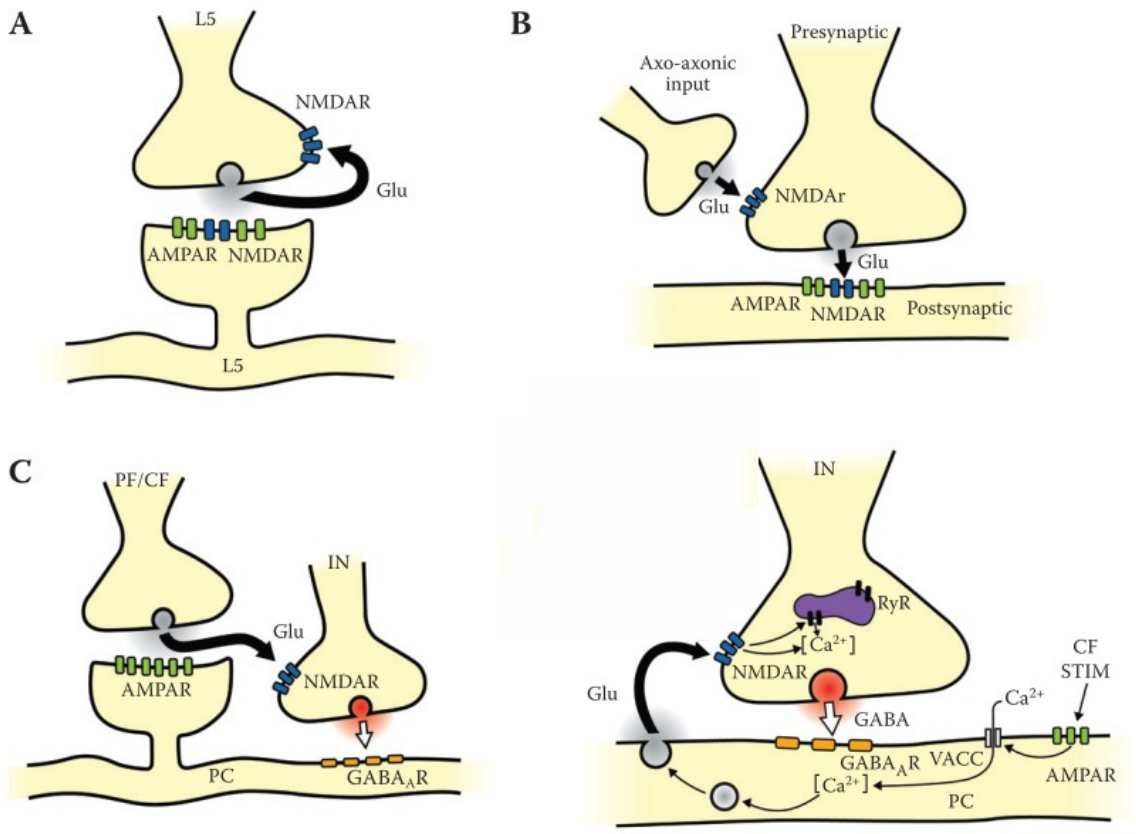

Figure 2: Presynaptic NMDARs can be activated by released glutamate in several ways. (A) Presynaptic autoreceptor activation in Layer 5. (B) Axo-axonic NMDAR activation. (C) Spillover-dependent NMDAR activation. High-frequency stimulation of cerebellar climbing fibres (CF) or parallel fibres (PF) results in glutamate pooling and saturation of juxtaposed excitatory amino acid transporters. Synaptic glutamate can diffuse out of the synapse (spillover) to activate presynaptic NMDARs on inhibitory interneurons. This leads to increased GABA release and postsynaptic $GABA_A$ receptor ($GABA_AR$) activation. (D) Retrograde release-dependent NMDAR activation. At the interneuron (IN)–Purkinje cell (PC) synapse, postsynaptic depolarization via CF stimulation (CF STIM) and AMPAR activation enables Ca^{2+} influx via voltage-activated Ca^{2+} channels (VACC) to induce the retrograde release of vesicular glutamate from the PC. Enhanced GABA release results from Ca^{2+} induced Ca^{2+} release from ryanodine-sensitive stores via ryanodine receptors (RyR). The released glutamate activates presynaptic NMDARs to enhance synaptic efficacy. Image: modified from Figure 14.1, "Presynaptic NMDAR activation by released glutamate" in [36].

2.3 Modelling synaptic currents

The time course of most synaptic conductances can be modelled with the product of two exponentials

$$g_{syn}(t) = \bar{g}_{syn} \cdot a \cdot (1 - e^{-t/\tau_1}) \cdot e^{-t/\tau_2}, \tag{1}$$

or the difference of two exponentials [44, 48, 57, 93],

$$g_{syn}(t) = \bar{g}_{syn} \cdot a \cdot (e^{-t/\tau_2} - e^{-t/\tau_3}), \text{ with } \tau_3 = \frac{\tau_2 \tau_1}{\tau_2 - \tau_1}, \tag{2}$$

or the dual exponential function defined in [97, p174]

$$g_{syn}(t) = \bar{g}_{syn} \cdot a \cdot (\tau_1 \cdot \tau_2) \cdot (e^{-t/\tau_2} - e^{-t/\tau_1})/(\tau_2 - \tau_1) \tag{3}$$

where t is elapsed time, $\bar{g}_{syn}$ is maximum conductance, a is the normalization factor, τ_1 is the rise time constant, and τ_2 is the decay time constant. The three equations were implemented as MATLAB^{TM} functions, and listed in the Appendix, Sections 8.5 and 8.6.

For this project I used the dual exponential function [97, p174] to model postsynaptic event currents. Typical event waveforms are shown in Figure 3.

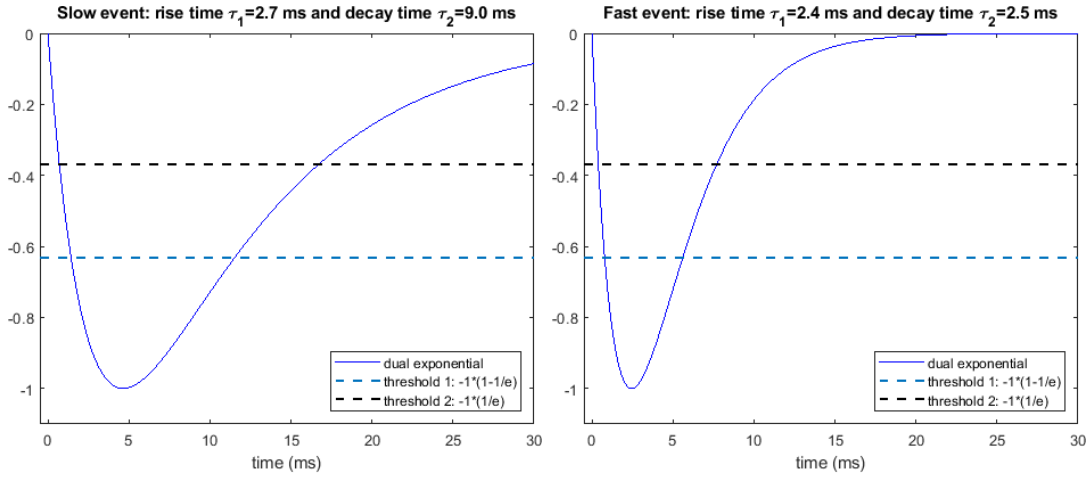

(a) (b)

Figure 3: Slow and fast event waveforms modelled with the dual exponential function and parameterised with the mean rise and decay time constants of slow or fast post drug events extracted from the data set in this report. Note: amplitude was normalised to -1.

When most ligand-gated ion channels mediating synaptic transmission open, such as AMPA-type glutamate receptors and γ-aminobutyric acid type A ($GABA_A$) receptors, their current-voltage relationship is approximately linear [93]. Synaptic current I_{syn} can be modelled at time t as an ohmic conductance g_{syn} multiplied by the driving force (membrane potential V minus reversal potential E_{syn}),

$$I_{syn} = g_{syn}(t)(V(t) - E_{syn}). \tag{4}$$

Synapses can be modelled as sources of current and not a conductance, i.e., without dependence on membrane potential V in Equation 4 by setting V to a constant. However, although outside the scope of this report, it should be noted that for inhibitory synapses, the inhibitory reversal potential can be close or even above the resting potential and, in that case, synaptic current becomes highly dependent the postsynaptic voltage [93, p144].

The parameters for Equations 1, 2, and 3 can be optimised by an iterative fitting procedure such that the mean squared error between function output and a typical synaptic

event is minimised. Equations with two exponentials are useful for making templates (exemplary waveforms) for event detection and classification, and for generating synthetic data. I used the dual exponential function [97, p174] for all template and synthetic data generation.

2.4 Event Detection and Classification

2.4.1 Introduction

Automatic algorithms for detecting events in electrophysiological signals have been based on combinations of one or more of the following methods:

1. a threshold for the amplitude or first derivative of the data [4, 9, 21, 29, 30, 67, 76],
2. templates, where a fixed template was compared to a recorded transient [77, 91, 105, 106],
3. cross-correlation between a template and the data set [1], or
4. deconvolution of the data with a template.

In general, there is no one best method; the best performing method will depend on the data, which may be populated with highly variable and overlapping waveforms. Hybrid methods that use correlation and mean squared error of the template versus the data, for example, can be effective, but they are quite slow. In general, I found that template based methods are less convenient to use, less robust to choice of parameters, and less accurate than neural network based methods, as described in Section 3.9.2.

2.4.2 Traditional methods

Detection and classification of are challenging problems in the presence of background noise, and overlapping events. Perhaps the simplest event detection method is to compare an amplitude threshold with data that has been filtered with a filter designed to reveal the events of interest [65]. However, templates based methods have been developed.

Miniature EPSC (mEPSC) events can be detected by extracting a representative mEPSC (the template) from the data, then calculating the cross-correlation of the template with the data [1]. Peaks in the cross-correlation function indicate points in the data with frequency components that match the template, as shown in Figure 4. The authors claimed that this method was not sensitive to levels of recording noise and to amplitude variability [1].

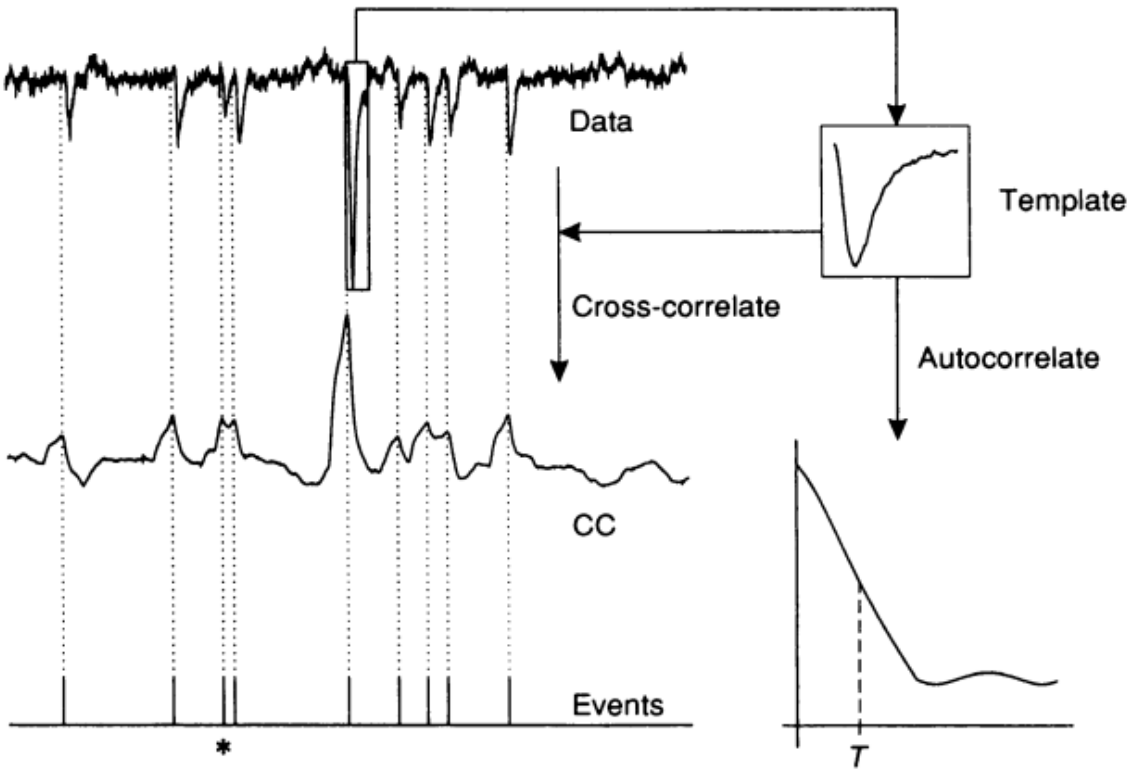

Figure 4: Event detection using cross-correlation. Image: [1].

Fixed-template techniques can be highly selective for the events of interest [28], and scaled templates have been used to reject corrupt or noisy evoked EPSCs [66]. But methods that use a template with only one or at most a few fixed amplitudes are not well suited for detecting highly variable spontaneous synaptic events [28].

A study by Clements and Bekkers [28] used a synaptic template with a variable amplitude for detecting spontaneous synaptic events. This method was found to be very selective for the synaptic events of interest, provided automatic threshold adjustment, and could be applied directly to data without additional filtering [28].

In general, template methods correlate the experimental trace with a template point by point and detect events when the correlation coefficient or the signal/noise ratio (SNR) exceeds a threshold [81]. While they work well for some data, deconvolution may provide higher temporal resolution than traditional methods, e.g. deconvolution of data with a template enabled reliable detection of pairs of EPSCs generated randomly at short time intervals [81].

2.4.3 Deconvolution

Deconvolution is an algorithm-based process used to reverse the effects of convolution on recorded data. The goal of deconvolution is to find the solution to a convolution equation:

$$h = (f * g) + \epsilon \tag{5}$$

where h is the recorded signal, and f is the signal of interest that was convolved with signal g, plus noise ϵ, before it was recorded.

The template fit algorithms proposed by [1], [28] and [53] incorporate information about the kinetics of PSCs. These algorithms show a low false event rate, but their temporal resolution is limited by template length [81]. But it should be noted that narrow templates with fast rise and decay constants can align well with high frequency fast events.

The duration parameter (template length) is a key determinant of sensitivity and specificity [28]; it was varied between 6.25 and 50 ms in [81].

Performance of the template method degrades when applied to traces with overlapping events [81]. To overcome limitations of template methods, Perniá-Andrade *et al.* developed a new method based on deconvolution [81]. This method was claimed to have high sensitivity and temporal resolution for detecting miniature and spontaneous PSCs [81]. In theory, if appropriate detection threshold is chosen, and if deconvolution converts a train of PSCs into a series of delta-like functions, the maxima of which can be precisely measured, then the frequency of excitatory events can be estimated with greater accuracy.

The deconvolution-based method exploits prior information about the time course of individual synaptic events. In [81], the recorded trace was the convolution of transmitter release and quantal conductance time series.

Their code for deconvolution is included in version 3.6.0 of BioSig [102] as `demo10.m`; the pseudocode for their `signal_deconvolution` function is listed in the Appendix, Section 8.7, Figure 24. Due to the way function arguments were parsed in their example, the data was not filtered at all. Also, the simple filter in `signal_deconvolution` caused a large ringing artefacts adjacent to the peaks in the deconvolved data. These artefacts (also known as "ripples") occur when the filtered output signal oscillates at a fading rate around a sharp transition in the input; they may cause multiple event detections where there was only one event.

2.4.4 Neural networks

The study of Artificial neural network (ANNs) has been partly inspired by biological learning systems composed of very complex webs of interconnected neurons. While biological neurons and their networks are indeed complex, ANNs are built from a densely interconnected set of simple units where each unit takes a number of real valued inputs and produces a single real valued output. The output from one unit may contribute to the input of another unit in another layer and in parallel with many other computations [74].

ANN based machine learning methods provide a way to approximate real valued, discrete valued, and vector valued target functions. These learning methods are robust to errors in the training data while algorithms such as backpropagation use gradient descent to tune network parameters to fit a training set of input-output pairs. Although ANNs have been the subject of intense interest during recent years, they have been successfully used since the 1980s: learning to recognise handwritten characters [61], spoken words [58], and faces [98]. An old survey of applications is provided by Rumelhart *et al.* [90].

Recent interest in "deep learning" has been driven by the availability of greater computational power and massive data sets. Deep learning refers to computational models composed of multiple processing layers that learn representations of data with multiple

levels of abstraction. Deep learning systems have improved the state-of-the-art in areas that include speech recognition, visual object recognition, object detection, drug discovery, and genomics. Neural networks with more layers and more artificial neurons can discover intricate structure in large data sets. While deep convolutional networks have brought breakthroughs in image, video, speech and audio processing, recurrent networks have led to a better understanding of sequential data such as text and speech [62].

Given that NNs are well suited to problems where the training examples are taken from noisy, complex sensor data [74], it would be surprising if NNs were not also well suited to classifying synaptic event waveforms with hundreds of features.

3 Methods

3.1 Software

I used MATLAB^{TM} 2018b [www.mathworks.com] and the Deep Learning Toolbox^{TM} (formerly Neural Network Toolbox^{TM}) [72] to implement software for event detection and classification; functions will appear in this font, `function_name`. However, only a shallow neural network with one hidden layer and 10 neurons was needed for the data in this report.

Clampfit^{TM} software (from Molecular Devices, LLC, San Jose, CA, USA) was used to inspect the whole cell patch clamp recording data and notes. All experimental protocols for this data are summarised by the Tables in Section 3.8 below.

3.2 Synthetic data

To simulate a recording that contains highly variable fast (glutamatergic) and slow (GABAergic) events I generated synthetic fast and slow event trains using Poisson, normal, uniform, and exponentially distributed random numbers and parameterised dual exponential functions. Sixty seconds of synthetic data is shown in Figures 5 and 6. For slow events, the base rise time constant was set at τ_r=1 ms and the base decay time constant was set at τ_d=15 ms. For fast events, the rates were set at τ_r=0.5 ms and τ_d=1.5 ms respectively. Random values were added to the base decay rates to generate events with highly variable decay kinetics. Actual mean decay time constants were much higher, 26.69 and 6.11 ms for slow and fast synthetic events respectively. Rise time constants were fixed.

Random values were also used to simulate variable inter event intervals and variable inter burst intervals. The MATLAB^{TM} code with parameters used to generate the synthetic data shown in Figures 5 and 6 may be found in Section 8.6.1 of the Appendix. Gaussian noise with a mean of zero and a small standard deviation was added to the synthetic data prior to computational testing, e.g. `data = data + randn(1,N) * 0.01` where N is data length.

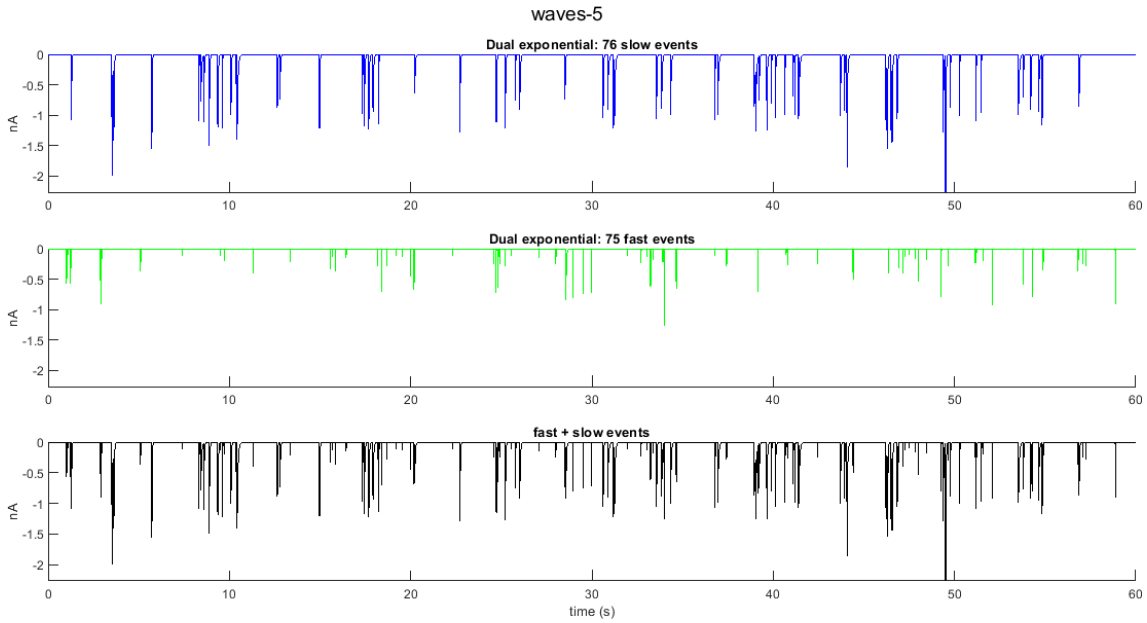

Figure 5: waves-5 synthetic data: Sixty seconds of slow event data (blue) was added to sixty seconds of fast event data (green) to create mixed data with with 151 potentially overlapping events. The base rise and decay time constants were (τ_r=1 ms, τ_d=15 ms) and (τ_r=0.5 ms, τ_d=1.5 ms) for slow and fast events respectively. Random values were added to the base decay rate for each event. Random inter event intervals determined the number of events.

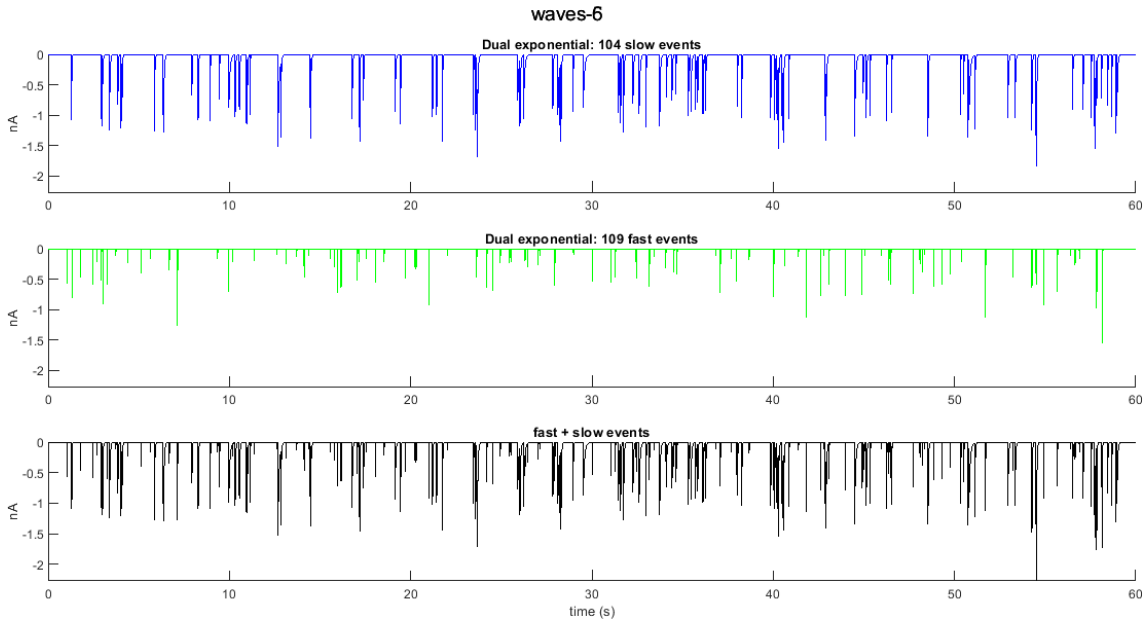

Figure 6: waves-6 synthetic data: Sixty seconds of slow event data (blue) was added to sixty seconds of fast event data (green) to create mixed data with 213 potentially overlapping events. The base rise and decay time constants were (τ_r=1 ms, τ_d=15 ms) and (τ_r=0.5 ms, τ_d=1.5 ms) for slow and fast events respectively. Random values were added to the base decay rate for each event. Random inter event intervals determined the number of events.

3.3 Real data

3.4 Transmembrane currents were recorded from the soma of dissociated Purkinje cells

Whole cell voltage clamp recordings were taken at the soma of a vibrodissociated [54] Purkinje cell (PC) with some synapses preserved, i.e. from climbing fibres (CF), basket cells (BC) in particular, but possibly also from stellate cells (SC), and even granule cells if the PFs were not completely removed. These recordings revealed fast and slow events.

1. The fast events were ESPCs mediated by AMPARs at the CF–PC synapse where presynaptic CF boutons release glutamate.

2. The slow events were IPSCs mediated by $GABA_A$ receptors at interneuron–PC synapses where presynaptic terminals release GABA [40].

Normally, ESPCs are also mediated by AMPARs at the PF–PC synapse where PF en passant boutons release glutamate. But the recordings were taken from a dissociated cell that might lack a dendritic tree. IPSCs can be mediated by $GABA_A$ receptors at BC-PC and SC-PC synapses.

3.5 Transmembrane current data was annotated by hand

The data set included an Excel spreadsheet for each file, one recording per file. Each spreadsheet contained rows of events and columns of features. Event detection and feature extraction were done by hand.

Event features included detection time, amplitude, rise time, decay time, area, and several more, but the additional features were assumed to be redundant and, therefore, excluded from further consideration. While events may be classified as slow or fast based on selected features, event detection time turned out to be the most useful feature. Given true event times, events can be extracted from unfiltered data as waveforms hundreds of features and used to train the classifier.

3.6 Pharmacology summary

- Bicuculline is a light-sensitive competitive antagonist of $GABA_A$ receptors; it blocks $GABA_A$ receptors and, therefore, slow events [56],

- DNQX is a competitive antagonist at AMPA and kainate receptors; it blocks AMPA receptors and, therefore, fast events [99],

- NMDA is an amino acid derivative that acts as a specific agonist at the NMDA receptor; it mimics the action of endogenous glutamate [56].

- Glycine, an inhibitory neurotransmitter in the CNS of mature animals, triggers chloride ion influx via ionotropic receptors, thereby creating an IPSC. This agent

also acts as a co-agonist, along with glutamate, facilitating an excitatory potential at NMDA receptors [56].

- Strychnine is a strong antagonist at ionotropic glycine receptors [56] that also also blocks GABA receptors [Personal communication: Professor Guy Moss, UCL].
- MK-801 is a noncompetitive antagonist (pore blocker) of NMDA receptors [56].
- Mg^{2+} is a voltage dependent blocker of NMDA receptors [16].

3.7 Lab Protocols

The data was generated by protocols designed to investigate the activity of presynaptic receptors; either NMDA or glycine receptors. The test results for NMDA receptors: NMDA receptors were activated by the co-agonists serine and glycine, and then blocked with either Mg^{2+} or MK801. The test results for glycine receptors on presynaptic CF terminals: glycine receptors were activated by applying higher concentrations of glycine alone. The test results for glycine versus NMDA receptors: glycine receptors were blocked partially with strychnine, but could not be blocked by Mg^{2+}. Each protocol was designed to either to confirm the event type or to modify event frequency by activating or blocking presynaptic receptors. Experimental results indicate that presynaptic glycine and NMDA receptors are present on the climbing fibre [Personal communication: Professor Guy Moss, UCL].

3.8 Summary of Protocols

Tag	time (s)	drugs	expected action
1	71.85	20 μM DNQX, 50 μM NMDA	block fast events, activate preNMDARs
2	129.20	20 μM DNQX, 50 μM bicc, 50 μM NMDA	block fast & slow events
3	213.30	20 μM DNQX, 50 μM NMDA	block fast events, activate preNMDARs

Table 2: Data file: DNQX-1="09n17004 v2.abf".

Tag	time (s)	drugs	expected action
1	37.45	20 μM DNQX, 50 μM NMDA	block fast events, activate preNMDARs
2	96.65	20 μM DNQX, 50 μM bicc, 50 μM NMDA	block fast & slow events
3	182.45	20 μM DNQX, 50 μM NMDA	block fast events, activate preNMDARs

Table 3: Data file: DNQX-2="09921004.abf".

The protocol in Table 4 was designed to reveal the action of glycine on GABAergic transmission. In this table, Org 25543 (Org) is a selective inhibitor of the GlyT2 transporter [24]. The distribution of GlyT2 is similar to the strychnine-sensitive glycine receptor (ss-GlyR), both are confined to the spinal cord and brain stem [24], except GlyT2 is also in the cerebellum.

GlyT2 is present in the terminals of glycinergic neurones where it maintains the supply of glycine to be taken up into presynaptic vesicles. GlyT1 is mostly present in glial cells and

is thought to be responsible for removing glycine from the synaptic cleft and terminating the action of glycine. Application of Org might reduce glycinergic drive by depriving the terminal of glycine. On the other hand it might cause potentiation by slowing the removal of glycine from the synaptic cleft [Personal communication: Dr David Benton, UCL].

After DNQX blocks AMPA receptors, all PSC events are expected to be GABA mediated.

Tag	time (s)	drugs	expected action
1	72.30	DNQX	block postsynaptic AMPARs, block fast events
2	359.65	Org	inhibit the GlyT2 transporter.
3	605.70	Org off	uninhibit the GlyT2 transporter
4	901.85	strych	block glycine receptors
5	1145.25	strych off	unblock glycine receptors

Table 4: Data file: DNQX-3="16405000.abf". Org: Org 25543, a selective inhibitor of the GlyT2 transporter.

Tag	time (s)	drugs	expected action
1	55.45	DNQX	block postsynaptic AMPARs, block fast events
2	304.30	DNQX strych	block glycine receptors
3	424.10	DNQX+strych+gly	block glycine receptors versus activate
4	545.75	DNQX+strych, gly off	block glycine receptors versus deactivate
5	728.15	DNQX, strych off	unblock glycine receptors
6	975.85	DNQX off	unblock postsynaptic AMPARs

Table 5: Data file: DNQX-4="16525000.abf".

Tag	time (s)	drugs	expected action
1	61.15	DNQX	block postsynaptic AMPARs, block fast events
2	305.15	DNQX 10 mM gly	activate glycine receptors
3	427.65	gly off	deactivate glycine receptors
4	608.35	strych 10 uM	block glycine receptors
5	724.20	strych 10 uM+gly 10 mM	block glycine receptors versus activate
6	857.85	gly strych off	unblock glycine receptors
7	1080.70	gly	activate glycine receptors
7	1204.95	gly off	deactivate glycine receptors

Table 6: Data file: DNQX-5="16526000.abf".

Tag	time (s)	drugs	expected action
1	65.15	DNQX	block postsynaptic AMPARs, block fast events
2	301.15	DNQX+NMDA	activate preNMDARs
3	480.05	DNQX+NMDA+gly	activate preNMDARs

Table 7: Data file: DNQX-6="16513000.abf".

Tag	time (s)	drugs	expected action
1	91.85	bicc	block slow events
2	245.90	Mg	block preNMDARs
3	368.05	NMDA, SER	activate preNMDARs
4	484.40	Mg off	unblock preNMDARs
5	604.40	NMDA/ser off	expect fewer fast events because preNMDARs not active and not able to mediate feedback from the postsynaptic cell, i.e. the Purkinje cell's soma.

Table 8: Data file: bicc-1="16630001.abf".

Tag	time (s)	drugs	expected action
1	63.25	bicc	block slow events
2	244.15	gly	coagonist for preNMDARs, expect more fast events
3	364.65	gly strych	strychnine blocks presynaptic glycine receptors
4	485.70	strych off	unblock presynaptic gly receptors
5	606.00	Mg	block preNMDARs
6	721.75	Mg off	unblock preNMDARs
7	844.35	gly off	coagonist for preNMDARs, expect less fast events

Table 9: Data file: bicc-2="16728001 v3.abf".

Tag	time (s)	drugs	expected action
1	61.85	bicc	block slow events
2	243.90	gly	activate presynaptic gly receptors
3	361.40	gly+Mg	activate presynaptic gly receptors, block preNMDARs
4	485.05	Mg off	unblock preNMDARs
5	605.60	+strych	block presynaptic glycine receptors
6	725.55	strych off	unblock presynaptic glycine receptors
7	844.85	gly off	-

Table 10: Data file: bicc-3="16728003.abf".

Tag	time (s)	drugs	expected action
1	75.90	bicc	block postsynaptic $GABA_A$Rs, block slow events
2	242.00	gly	activate glycine receptors
3	362.45	gly+strych	block glycine receptors
4	483.85	strych off	unblock glycine receptors
5	602.10	gly off	deactivate glycine receptors
6	782.85	TTX	block Na+ channels, block action potentials
7	903.10	TTX+gly	block Na+ channels, activate presynaptic gly receptors
8	1022.95	TTX off	unblock Na+ channels
9	1143.35	gly off	deactivate glycine receptors

Table 11: Data file: bicc-4="16922000.abf".

Tag	time (s)	drugs	expected action	slow %	fast %
0	0	none	none	-	-
1	298.75	10 μM NMDA on	increase preNMDAR	-	-
2	358.95	10 μM NMDA off	decrease preNMDAR	-	-

Table 12: Data file: NMDA-1="08603001.abf".

3.9 Event detection and classification

3.9.1 A template method for event detection and classification

This template method is similar to [44], which was based on work by Jonas *et al.* [53], and Clements and Bekkers [28], but it is relatively fast, i.e. the mean squared error of the templates versus unfiltered data is only calculated once per event detection time point and template shapes are not optimised in any way during classification. Event times were detected by amplitude threshold detection on filtered data.

Electrodes record signals due to synaptic currents and action potentials [43]. Synaptic currents are relatively slow and can be separated with a bandpass filter. To facilitate synaptic event detection, the first step was to "flatten" the signal by filtering out the low frequency content [85] and remove noisy high frequency content.

The filter was constructed with a second order Butterworth filter `butter` from the Signal Processing Toolbox^{TM}. The ideal aim of this filter is to have uniform sensitivity to the wanted frequencies, and zero sensitivity to unwanted frequencies, i.e. completely reject unwanted frequencies [20]. In practice the frequency response of the Butterworth filter is maximally flat in the passband, say 100 to 600Hz, it attenuates rapidly in the stopband (less than and greater than the passband) [13]. While the bandpass was set to 100 to 600Hz for slow and fast event detection, the best cut-off frequencies depend on the application, i.e. the rise and decay time constants of the events of interest.

However, causal filters usually introduce phase distortions which may greatly alter waveform shapes and peak times. Distortions can be greatly reduced by using a non-causal filter that removes noise without introducing phase lag [86]. The Signal Processing Toolbox^{TM} includes the function `filtfilt` for implementing a non-causal filter. The `filtfilt` function performs zero-phase digital filtering by processing the input data in the forward and reverse directions [79]. This preserved the peak time of each event. Multiple event detection points, if any, due to small amounts of ringing around the peak were consolidated into one detection time point at the peak.

Preliminary threshold estimates were a negative multiple of the standard deviation of the filtered data, then the actual threshold was set after a close visual inspection was made of the threshold versus about 10 seconds of filtered data to ensure that all or nearly all event peaks crossed the threshold.

Visual inspection was necessary because setting the threshold for detection involves a sensitive trade-off between false positives and false negatives [11]. A higher threshold may prevent more false positives, but then more true events might be discarded.

Of course an automatic threshold can be calculated as a multiple K of the estimated standard deviation σ of noise that is assumed to be normally distributed, i.e. threshold = $K \times \sigma$, where K is a constant [89]. Another possibility is a threshold based on the median absolute deviation (MAD) [32, 85]. This threshold is a multiple of the MAD

$$Thr = K \times \sigma_n; \qquad \sigma_n = \frac{\text{median}|X|}{0.6745} \tag{6}$$

where $K = 4$, X is the filtered data, and the denominator 0.6745 is derived from the inverse of the cumulative distribution function for the standard normal distribution evaluated at 0.75 [89]. In other words, the area under the curve left of 0.6745 standard deviations equals 0.75.

MAD is based on the median and, therefore, is much less sensitive to the firing rate, large amplitude events, and artefacts than the traditional standard deviation estimate of noise. Nonetheless, synaptic current events are highly variable, especially in terms of amplitude. Consequently, even though MAD is a more robust estimate of background noise, it was too sensitive to be useful for event detection.

Many events are tiny and a threshold that is just a little too high will cause too many false negatives. For the data in this report, a high threshold would have biased results in favour of detecting large amplitude slow events and, therefore, it was necessary to set the final threshold by visual inspection of the filtered data. Then after detection, events in unfiltered data were compared with templates.

To create slow and fast templates I used a dual exponential function parameterised with the mean rise and decay time constants and amplitudes of typical events to construct the example templates shown in Figure 7. For classification of events, I used the mean rise and decay time constants taken from the annotations in the Excel spreadsheet files that were included with the data. Template length was adjusted for sensitivity and selectivity. Template amplitudes were standardised to -1 to nullify the issue of baseline drift in some recordings (unfiltered data) versus the MSE for different templates.

Templates were more useful than mean waveforms extracted from clustered waveform data because template parameters are explicit and can be easily adjusted to improve event detection and classification, e.g. a faster and shorter length template may provide better temporal resolution for high frequency events.

In summary, two templates (slow and fast) were peak aligned with the unfiltered data at each event time detection point. Classification was by mean squared error (goodness of fit) for each template.

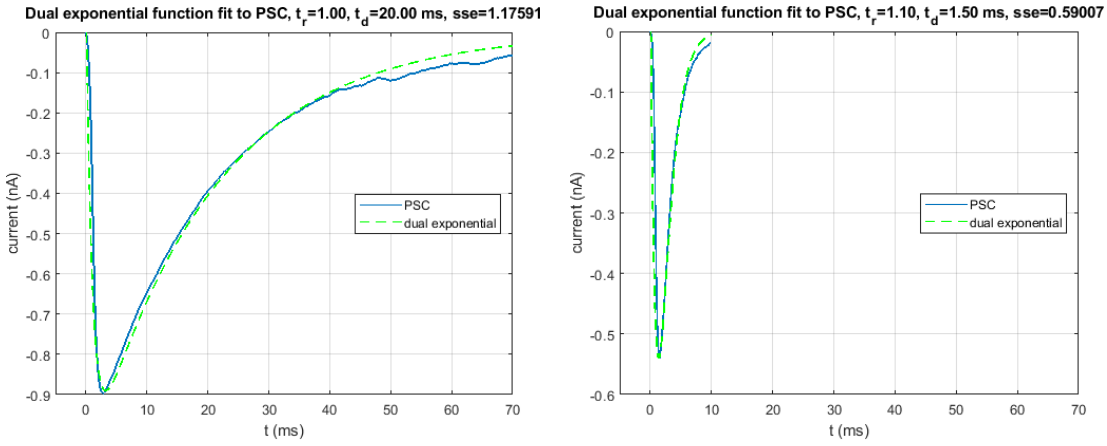

(a) Slow (b) Fast

Figure 7: Dual exponential function templates fit to the mean of clustered PSC waveforms recorded after application of DNQX and bicuculline respectively: (a) slow: $\tau_r = 1$ ms, $\tau_d = 20$ ms. (b) fast: $\tau_r = 1.1$ ms, $\tau_d = 1.5$ ms. Here, a typical waveform is the mean of a cluster of similar post drug events, not all events. Data files: DNQX-2="09921004.abf" and bicc-2="16728001 v3.abf".

		slow events		fast events	
file pair	event count	mean τ_{rise}	mean τ_{decay}	mean τ_{rise}	mean τ_{decay}
d1,b1	62	2.13	8.66	0.07	2.34
d2,b2	51	2.28	8.19	0.11	3.59
d3,b3	83	3.85	10.03	0.08	1.50
d4,b4	227	2.56	8.93	0.06	2.32

Table 13: Mean rise and decay times taken from the Excel spreadsheets included with the real data. All of these events were post drug and exclusively of one type. File pairs d1,b1, ..., refer to DNQX file 1 and bicuculline file 1, and so on.

3.9.2 Neural networks for event classification

The Deep Learning Toolbox™ function `patternet` can be parameterised in many ways, including the number of neurons, number of hidden layers, training function (`trainscg, trainlm, trainbr`) and transfer function (`logsig, tansig, softmax`).

For this report I set the number of hidden layer neurons to 30, and the number of hidden layers to 1. However, the choice of network architecture for pattern recognition problems involves trade-offs. Over a limited range more neurons can improve classification accuracy and enable the network to solve more difficult problems, but more neurons require more computation and may overfit the data. More layers require more computation, but a network with more layers might be able to solve complex problems more efficiently [72].

I tested three training functions from the Deep Learning Toolbox™.

- Scaled conjugate gradient (SCG) backpropagation `trainscg`: This is the default training function. It updates weight and bias values according to the scaled conjugate gradient method.

- Levenberg-Marquardt (LM) backpropagation `trainlm`: This function updates weight and bias values according to the Levenberg-Marquardt optimization algorithm [71]. Its application to neural network training is described in [45] and [46, pp12-19]. It is often the fastest backpropagation algorithm in the Deep Learning toolbox™. Although recommended as a first-choice supervised algorithm, it requires more memory than other algorithms [72].

- Bayesian regularization (BR) backpropagation `trainbr`: This function updates the weight and bias values according to Levenberg-Marquardt optimization. It minimizes a combination of squared errors and weights, and finds the combination that produces a network that generalises well using a process known as Bayesian regularization [72].

I chose the SCG training function because it scaled well to high dimensional data. In contrast, LM and BR were very slow.

Transfer functions calculate a layer's output from its input. There are several options.

- Log-sigmoid transfer function `logsig`: $logsig(n) = 1/(1 + e^{-n})$ returns a value in the range of 0 to 1.

- Hyperbolic tangent sigmoid transfer function `tansig`: $tansig(n) = 2/(1+e^{-2*n}) - 1$ returns a value in the range of -1 to 1.

- Soft max transfer function `softmax`: $a = softmax(n) = exp(n)/sum(exp(n))$, returns a value in the range of 0 to 1, where n is a vector of values presented to the output layer, one for each class. So, for each vector n, this function returns the posterior probabilities for each class such that they sum to 1, e.g. 0.9 and 0.1 for the classes slow and fast respectively.

For this project, the neural network's hidden layer used the `tansig` transfer function, and the output layer used the `softmax` function, as shown in Figure 8.

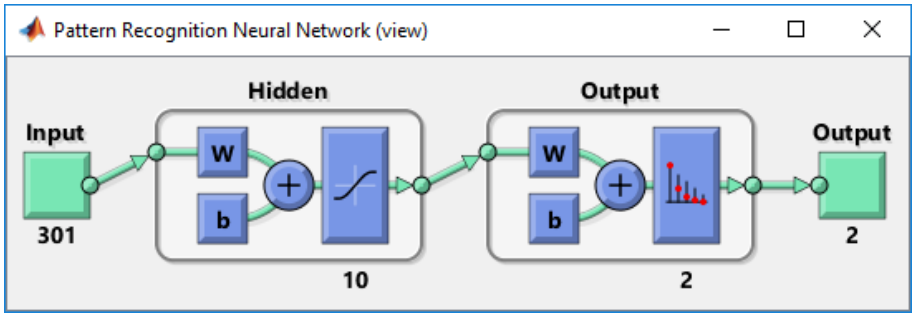

Figure 8: Neural network diagram: this network accepts inputs with 301 features, feature values are associated with a weight vector and a bias **b** that the input layer to the hidden layer, the hidden layer is composed of 10 artificial neurons with sigmoidal activation functions, weight vectors and a bias connect the hidden layer to the output layer, the output layer uses a softmax function to output the posterior probability that the input belongs to each class. Image: generated by the function `view(net)` from the Deep Learning Toolbox™.

4 Results

4.1 Detection and classification of events

For each data file, the number of true positives (TP), false positives (FP), and false negatives (FN) were counted. Their respective rates were calculated as follows

$$TPR = TP/n \tag{7}$$

$$FPR = FP/n \tag{8}$$

$$FNR = FN/n \tag{9}$$

$$\tag{10}$$

where n is the number of ground truth slow and fast events.

Overall prediction accuracy (acc) was calculated as the total number of true positives divided by the total number of predictions (TP+FP) plus the number of false negatives (FN):

$$acc = TP/(TP + FN + FP). \tag{11}$$

True negatives (TN) were not considered because in cases where events were detected versus filtered data, almost all data points would correspond to TNs and any measure of accuracy that included TNs would be inflated, misleading, and not useful.

4.1.1 Template method event detection and classification of events in synthetic data

Synthetic data was generated with the same event parameters for both synthetic data files, so the template method used those parameters for template generation, as shown in Table 14.

event	template length	amplitude	rise time constant (ms)	decay time constant (ms)
slow	70.1	-1	1.0	15.0
fast	14.1	-1	0.5	1.5

Table 14

Template method results for waves-5 and waves-6 synthetic data are shown in Figures 9 and 10, and their rates are reported in Tables 15 and 16 respectively.

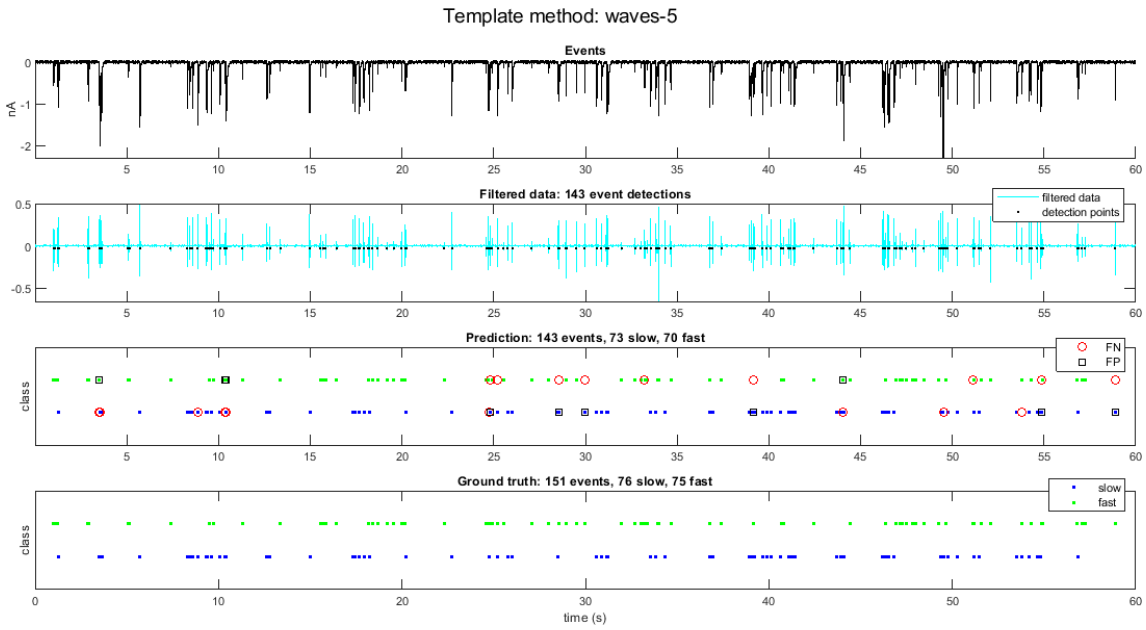

Figure 9: Template method: event detection and classification versus ground truth for 60 seconds of waves-5 synthetic data; the prediction accuracy was 0.83.

data file	time (s)	event type	GT count	GT Hz	TPR	FNR	FPR
waves-5	60	slow	76	1.27	0.88	0.12	0.08
waves-5	60	fast	75	1.25	0.88	0.12	0.05
waves-5	60	both	151	2.52	0.88	0.12	0.07

Table 15: Rates for template method event detection and classification of 60 seconds of waves-5 synthetic data. The overall prediction accuracy was 0.83.

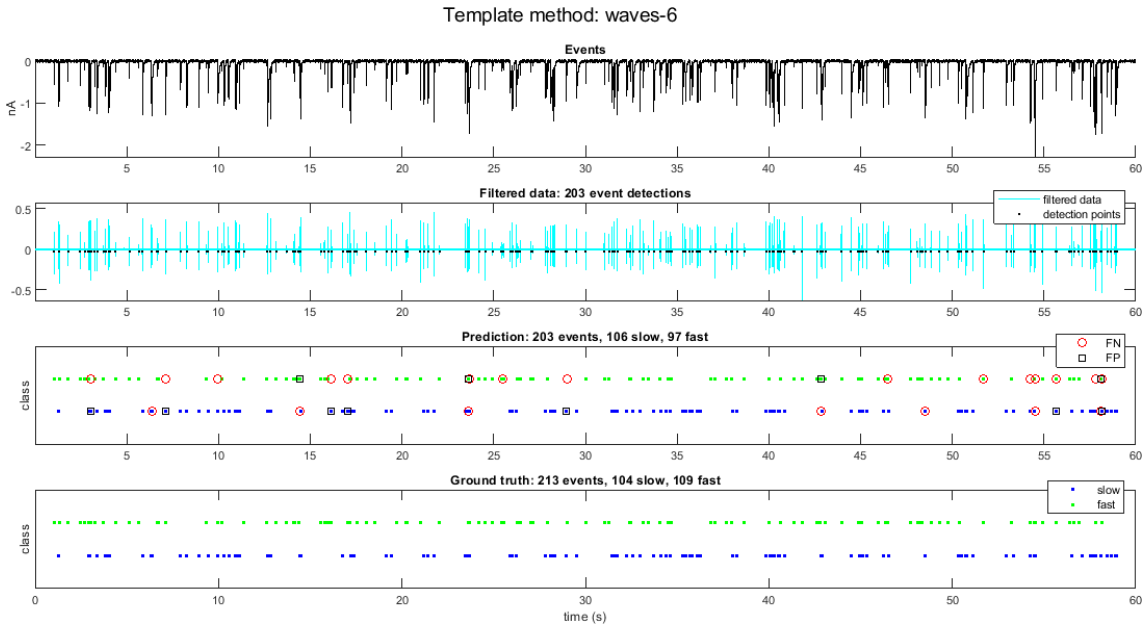

Figure 10: Template method: event detection and classification versus ground truth for 60 seconds of waves-6 synthetic data; the prediction accuracy was 0.85.

data file	time (s)	event type	GT count	GT Hz	TPR	FNR	FPR
waves-6	60	slow	104	1.73	0.93	0.07	0.07
waves-6	60	fast	109	1.82	0.85	0.15	0.04
waves-6	60	both	213	3.55	0.89	0.11	0.05

Table 16: Rates for the Template Method event detection and classification of 60 seconds of waves-6 synthetic data. The overall prediction accuracy was 0.85.

4.1.2 Neural network event detection and classification of events in synthetic data

The mean accuracy for the NN given ground truth event detection times over 30 trials was 96.62% (σ=1.24%) on waves-5 synthetic data, and 96.10% (σ=0.81%) on waves-6 synthetic data. These rates indicate the maximum accuracy for this network on these data sets.

Figures 11 and 12 show the results from a single trial. Tables 17 and 18 report the rates; the main point being that threshold based event detection on filtered data reduced the mean overall accuracy from about 96% to about 90%.

Ground truth (GT) was used to score predicted event times and classes. Predicted events times within 5 ms of GT event times were "matched"; they were true positives that accrued to the true positive rate (TPR). GT events that were not matched were false negatives that accrued to the false negative rate (FNR). Predicted event times not within 5 ms of GT event times were recorded as false positives and accrued to the false positive rate (FPR).

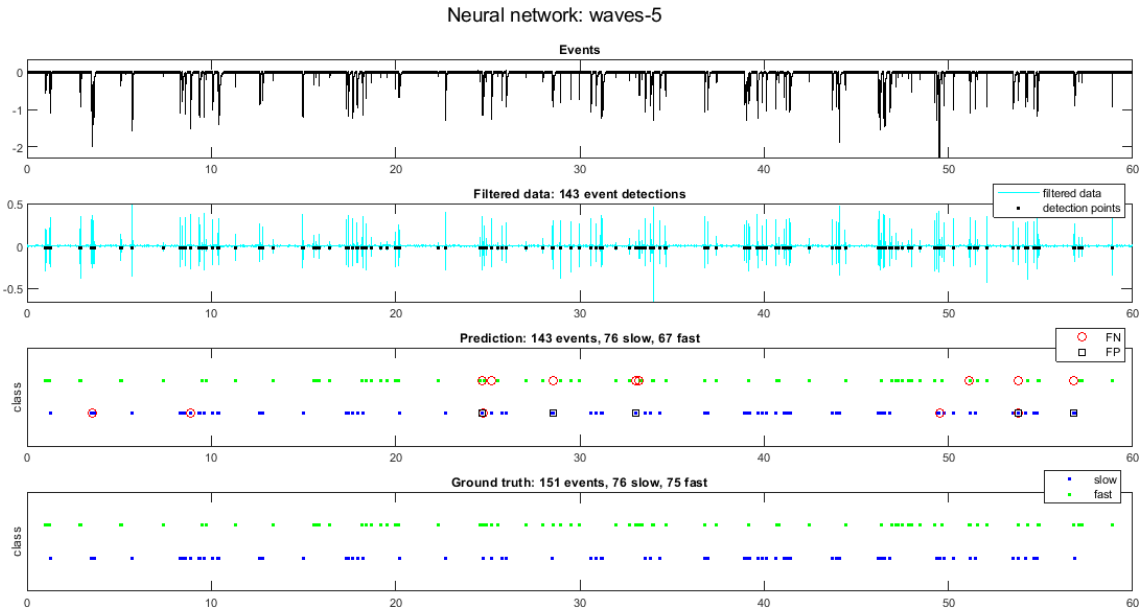

Figure 11: Neural network method: event detection and classification versus ground truth for 60 seconds of waves-5 synthetic data. These are the results from one trial. False negative (FN) and false positive (FP) predictions are indicated by red circles and black squares respectively.

data file	time (s)	event class	GT count	GT Hz	TPR	FNR	FPR
waves-5	60	slow	76	1.27	0.94	0.06	0.01
waves-5	60	fast	75	1.25	0.93	0.07	0.01
waves-5	60	both	151	2.52	0.94	0.07	0.02

Table 17: Rates for neural network event detection and classification of 60 seconds of waves-5 synthetic data. The mean rates are based 30 trials. The mean overall prediction accuracy was 0.92 (σ=0.01).

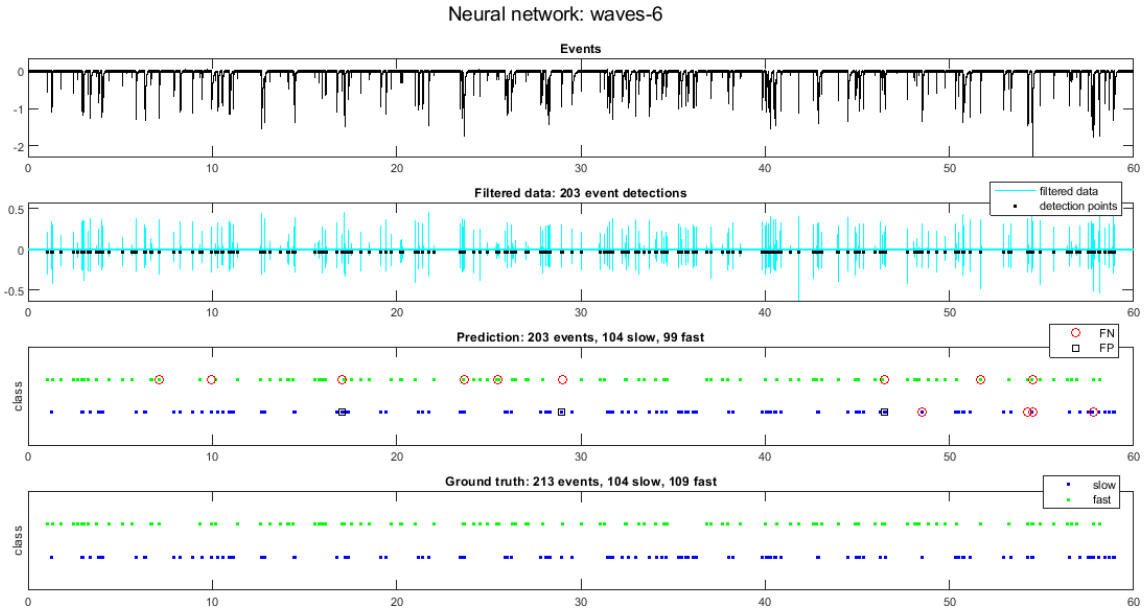

Figure 12: Neural network method: event detection and classification versus ground truth for 60 seconds of waves-6 synthetic data. These are the results from one trial. False negative (FN) and false positive (FP) predictions are indicated by red circles and black squares respectively.

data file	time (s)	event class	GT count	GT Hz	TPR	FNR	FPR
waves-6	60	slow	104	1.73	0.95	0.05	0.04
waves-6	60	fast	109	1.82	0.92	0.08	0.07
waves-6	60	both	213	3.55	0.93	0.07	0.06

Table 18: Rates for neural network event detection and classification of 60 seconds of waves-6 synthetic data. The mean rates are based 30 trials. The mean overall prediction accuracy was 0.89 (σ=0.01).

4.2 Neural networks

The neural network method was relatively easy to use as there were few parameters to set, and it performed better than the template method on synthetic data, so the neural network was chosen for more tests and analysis of real data.

4.2.1 Neural networks on selected features of real data

For the first test on real data, each event was a set of selected ground truth features (amplitude, rise time constant, decay time constant, and area). Mean feature values are shown in Table 19.

event type	amplitude (nA)	rise time (ms)	decay time (ms)	area (nA^2)
slow	0.32	2.71	8.95	3.46
fast	0.08	2.44	2.48	0.29

Table 19: Mean post drug hand annotated feature values for the four file pairs (D1,B1)..(D4,B4)

.

Figures 13 and 14 show the post drug mean and standard deviation of selected features in eight files. The kinetics of slow and fast events do indeed overlap. Greater of overlap of feature values was expected to reduce classification accuracy. For example, the greatest overlap of post drug decay time constants was for file pair (D2,B2), as shown in Figure 13(b). Indeed, classification accuracy of (D2,B2) post drug events was consistently the lowest.

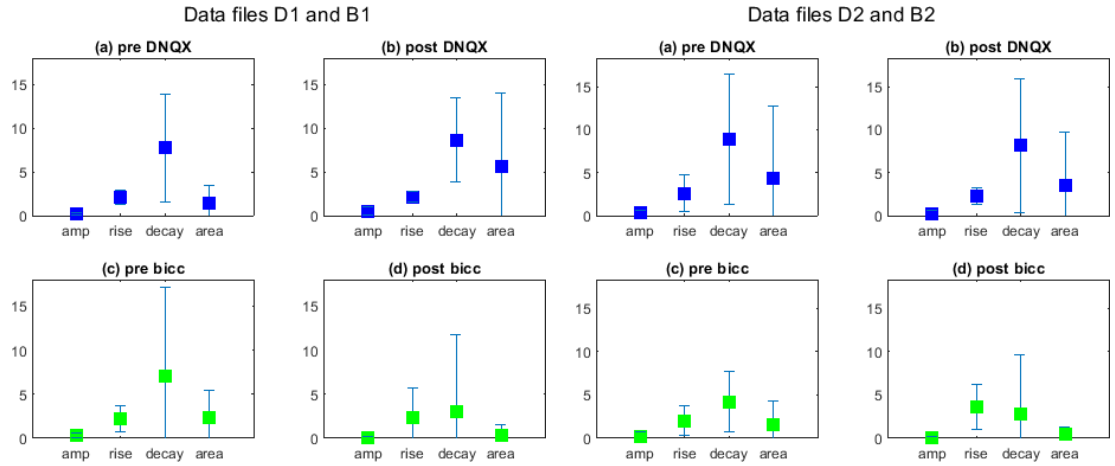

(a) File pair (D1,B1) (b) File pair (D2,B2)

Figure 13: The mean and standard deviation of selected features post DNQX or bicc in two pairs of data files. Pre drug events are mixed, while post drug events should be of one type. Units: amplitude "amp" (nA), rise and decay times (ms), area (nA^2).

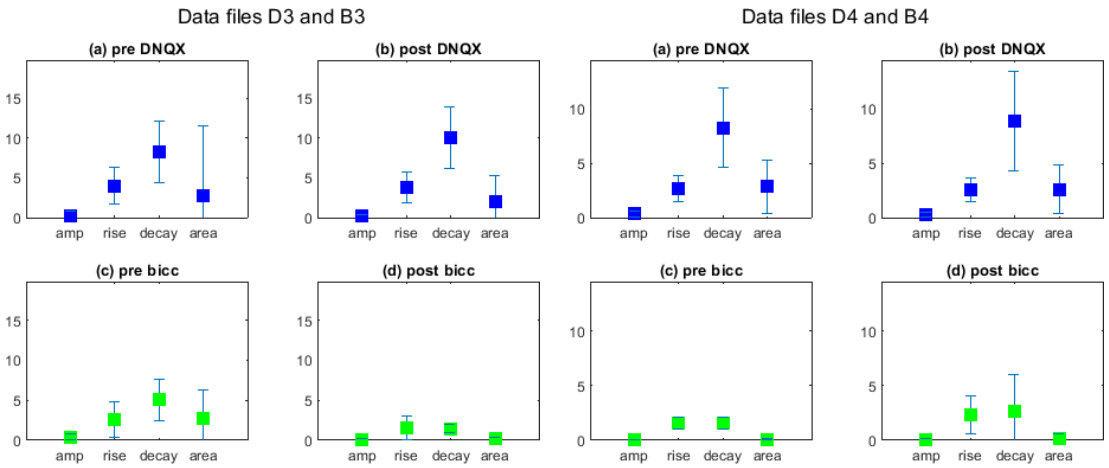

(a) File pair (D3,B3) (b) File pair (D4,B4)

Figure 14: The mean and standard deviation of selected features post DNQX or bicc in two pairs of data files. Pre drug events are mixed, while post drug events should be of one type. Units: amplitude "amp" (nA), rise and decay times (ms), area (nA^2).

The network was trained on equal numbers of "labelled" example events from each pair of data files. All events used for training were detected after the application of DNQX or bicuculline and, therefore, all of the events in each half of the training set should be of one type.

The number of examples from each pair of files was 62 from (D1,B1), 51 from (D2,B2), 87 from (D3,B3), and 227 from (D4,B4). The data from each pair of files was partitioned into training (70%), validation (15%), and test (15%) sets. The number of slow and fast events in the sets was equal for every trial, so the classifier always had a 50% chance of guessing correctly.

4.2.2 Classification of events based on selected features

The Deep Learning Toolbox^{TM} function `patternnet` has many parameters and options, including the number of hidden layers, number of neurons in each hidden layer, the training function, and the transfer function for the output layer. However, only a few parameters were explored.

This NN had a 10 node hidden layer. The accuracy of three training functions is shown in Table 20: scaled conjugate gradient (SCG), Levenberg-Marquardt (LM), and Bayesian regularisation (BR). This table shows that the mean accuracy over 30 trials was greater than 90% for all file pairs except (D2,B2). While the performance of the BR training function appears to be superior, especially on (D2,B2), its running time was about 10 times greater than the other two on this data. The LM training algorithm might be a good first choice for data with a small number of features, e.g. 4, but its running time increases greatly with the number of features. In contrast, SCG, the default training function, scales well with the number of features, e.g. runtime on data with 4 features versus 201 features (the entire waveform) was about the same.

Although SCG accuracy was only 90.18% on the selected features data, it was relatively

fast and performed well on extracted waveform data with hundreds of features. Annotating features by hand is of course very time consuming, so a machine learning method "extracts" features automatically is very useful. Consequently the SCG training function was chosen for all subsequent tests.

	Files D1, B1		Files D2, B2		Files D3, B3		Files D4, B4		All Files	
function	μ (%)	σ	μ (%)	σ	μ (%)	σ	μ (%)	σ	μ (%)	σ
SCG	91.72	5.44	75.62	11.19	98.57	0.93	94.82	2.24	**90.18**	4.95
LM	95.38	2.04	84.12	7.67	98.84	0.57	96.47	0.68	93.70	2.74
BR	97.26	1.03	95.78	1.95	99.24	0.42	99.05	0.93	97.83	0.93

Table 20: Accuracy of a neural network with 10 hidden nodes using three training functions over 30 trials on four pairs of data files with ground truth event time and features. Bayesian regularization (BR) had the best mean accuracy over all files, but its runtime was about 100 seconds versus about 10 seconds for scaled conjugate gradient (SCG) and Levenberg-Marquardt (LM). Note: these times were for a NN with a 10 node hidden layer; the examples had four selected hand annotated features, i.e. amplitude, rise time, decay time, and area.

4.2.3 Classification with the SCG training function on waveforms extracted from post drug data

This neural network had a 10 node hidden layer and used the default training function scaled conjugate gradient (SCG); the input was a set of extracted waveforms, 201 data points each. As shown in Table 21 21, this NN had the highest mean accuracy over 30 trials, 98.69% (σ=1.91) versus Table 20.

	Files D1, B1		Files D2, B2		Files D3, B3		Files D4, B4		All Files	
function	μ (%)	σ	μ (%)	σ	μ (%)	σ	μ (%)	σ	μ (%)	σ
SCG	98.25	1.96	97.52	4.58	99.66	0.42	99.33	0.66	**98.69**	1.91

Table 21: Accuracy of a neural network with 10 hidden nodes using using the SCG training functions over 30 trials on four pairs of data files with ground truth event times. The runtime for SCG was under 10 seconds. In contrast, LM and BR were not fast enough on high dimensional data to be useful.

4.2.4 Classification of waveforms extracted from pre DNQX and pre bicc data

Figures 15, 16, and 17 show recordings taken before and after a drug (receptor antagonist) was washed in. Consequently, a mixture of slow and fast events were recorded pre drug, but only slow or fast events after the drug.

Event detection time points were by ground truth annotations (from the Excel spreadsheets). A waveform of length 201 data points long and peak aligned at data point 101 was extracted from unfiltered data with reference to a detection point in the time series. Extraction with reference to ground truth detection time points greatly facilitated accurate

classification accuracy. Tables 22 and 23 report the rates for pre drug and post DNQX events.

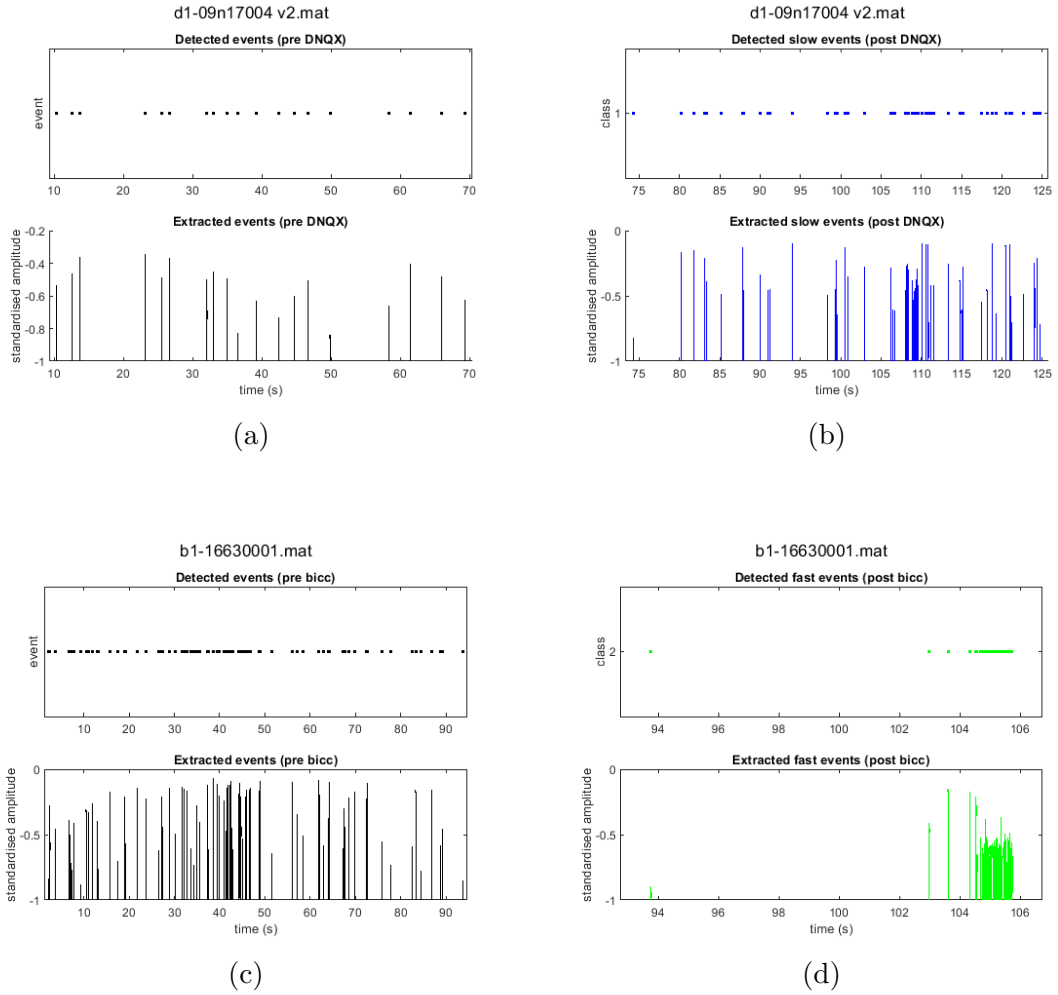

Figure 15: Hand detected event times and their waveforms, 201 data points each: (a) mixed pre DNQX events, (b) 62 slow post DNQX events, (c) mixed pre bicc events, (d) 62 fast post bicc events. The fast events in (d) are mostly in one high frequency burst. File pairs (D1,B1).

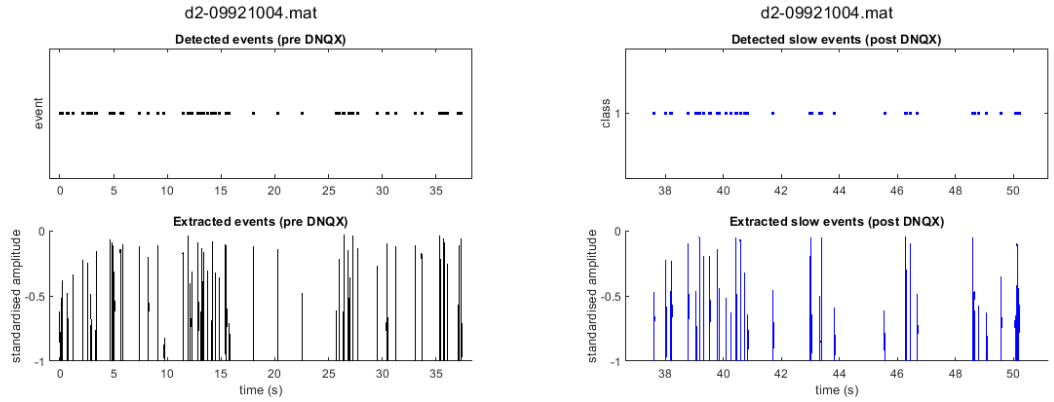

(a)

(b)

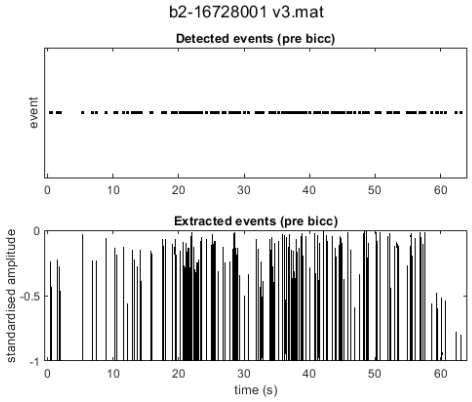

(c)

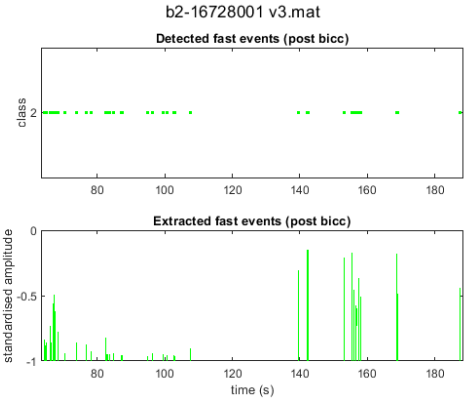

(d)

Figure 16: Hand detected event times and their waveforms, 201 data points each: (a) mixed pre DNQX events, (b) 51 slow post DNQX events, (c) mixed pre bicc events, (d) 51 fast post bicc events. File pairs (D2,B2).

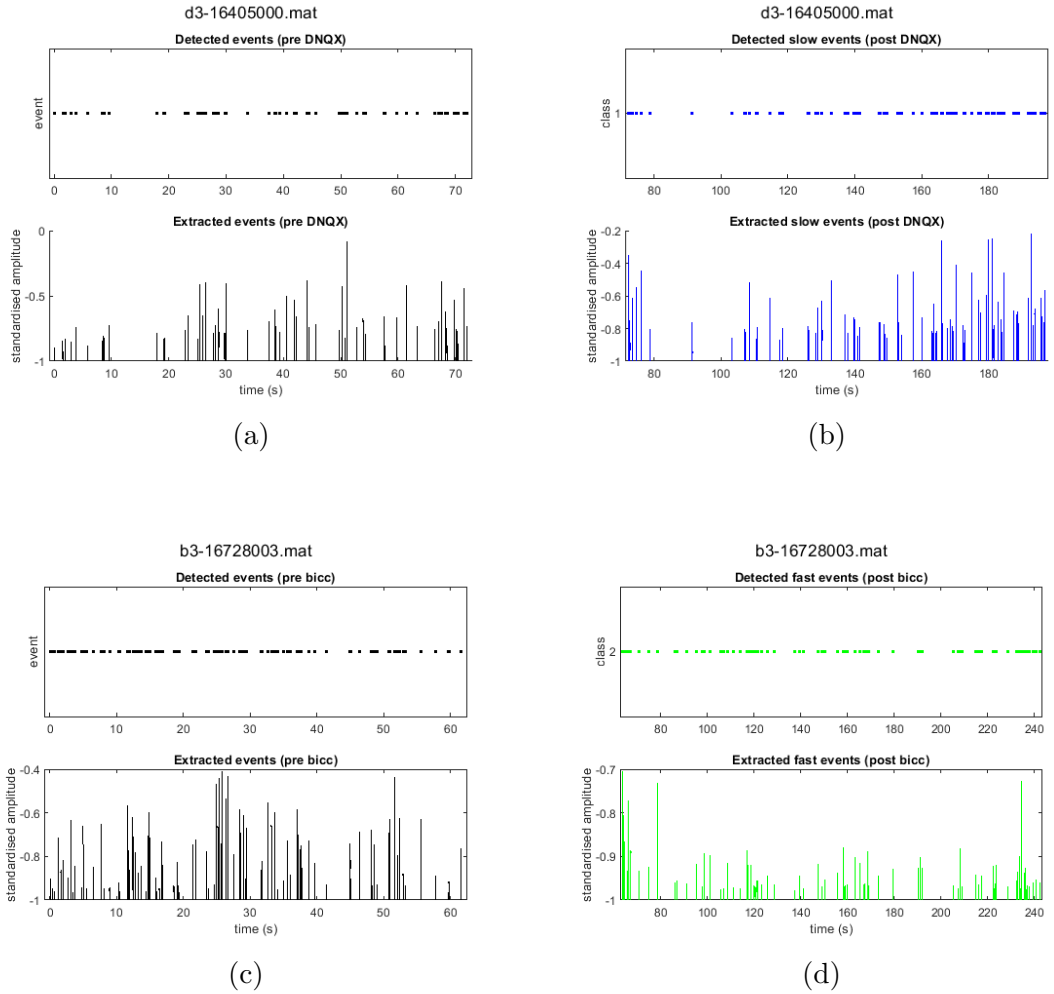

Figure 17: Hand detected event times and their waveforms, 201 data points each: (a) mixed pre DNQX events, (b) 87 slow post DNQX events, (c) mixed pre bicc events, (d) 87 fast post bicc events. File pairs (D3,B3).

	Pre DNQX Events							
	percent			count		Hz		seconds
file	μ slow	μ fast	σ	μ slow	μ fast	μ slow	μ fast	time window
D1	89.3	10.7	4.7	21.4	2.6	0.36	0.04	59.1
D2	91.9	8.1	4.2	78.1	6.9	2.09	0.18	37.4
D3	91.5	8.5	2.0	54.0	5.0	0.75	0.07	71.8
mean	90.9							

Table 22: Classification of pre DNQX events over 30 trials. On average, about 90.9% were slow events. A neural network with 10 hidden nodes using the SCG training function was trained on ground truth post DNQX and bicc events from file pairs (D1,B1), (D2,B2), (D3,B3); it classified the pre DNQX events in files D1, D2, D3 respectively.

	Pre bicc Events							
	percent			count		Hz		seconds
file	μ slow	μ fast	σ	μ slow	μ fast	μ slow	μ fast	time window
B1	58.0	42.0	5.1	54.5	39.5	0.60	0.43	91.5
B2	45.7	54.3	11.1	102.8	122.2	1.64	1.95	62.6
B3	48.6	51.4	3.3	50.6	53.4	0.83	0.87	61.3
mean	50.8							

Table 23: Classification of pre bicc events over 30 trials. On average, about 50.8% were slow events. A neural network with 10 hidden nodes using the SCG training function was trained on ground truth post DNQX and bicc events from file pairs (D1,B1), (D2,B2), (D3,B3); it classified the pre bicc events in files B1, B2, B3 respectively.

4.2.5 Classification of waveforms extracted from pre and post NMDA data

Figures 18 and 19 show the results of event detection and waveform extraction from pre and post NMDA data. Event detection times were by amplitude threshold set by visual inspection versus filtered data. Tables 24 and 25 report the classification results.

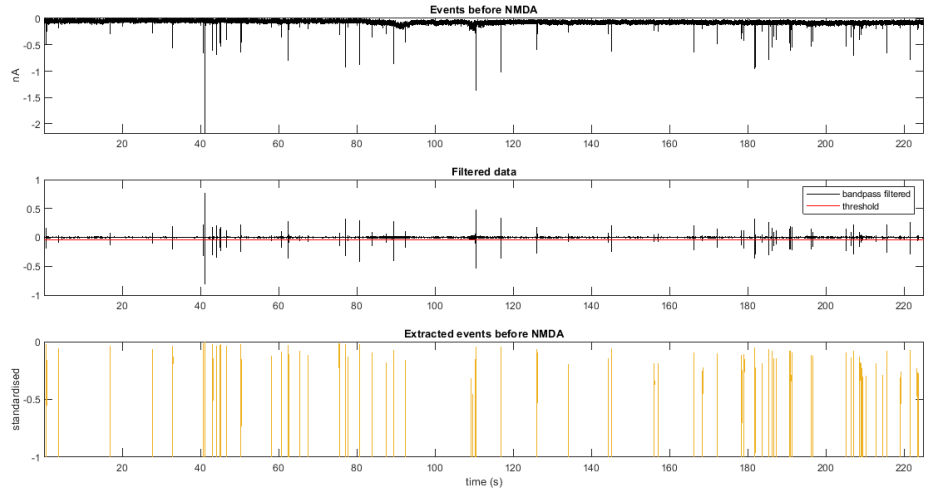

(a) 225 seconds

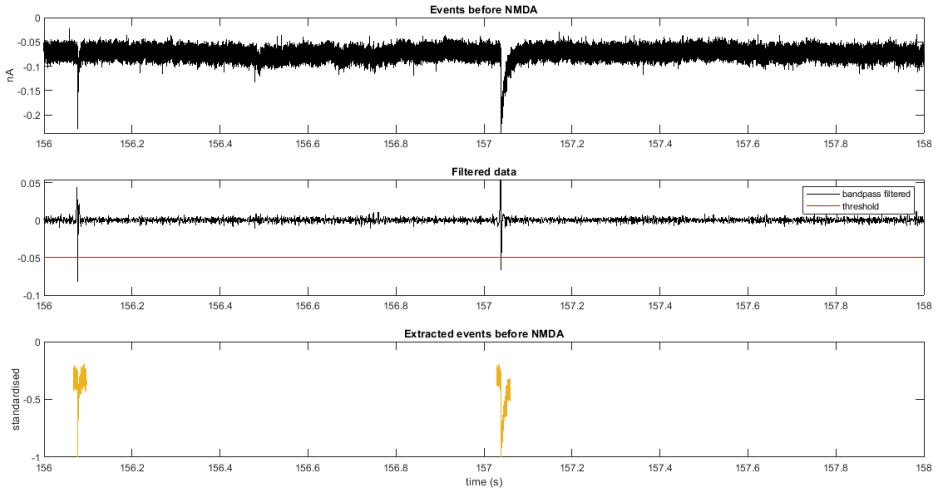

(b) Zoomin: 2 seconds

Figure 18: Threshold based event detection: (a) Events before NMDA: the first 225 seconds of the recording shows mixed events before the application of any drugs, i.e. NMDA was washed in at 298.75 seconds. Filtered data: bandpass filtered data (black) and event detection threshold (red). Extracted events: each waveform (orange) is peak aligned, i.e. 100 data points before and after the peak (minimum amplitude). (b) Shows details of a 2 second window. Threshold = -0.05 (set by visual inspection).

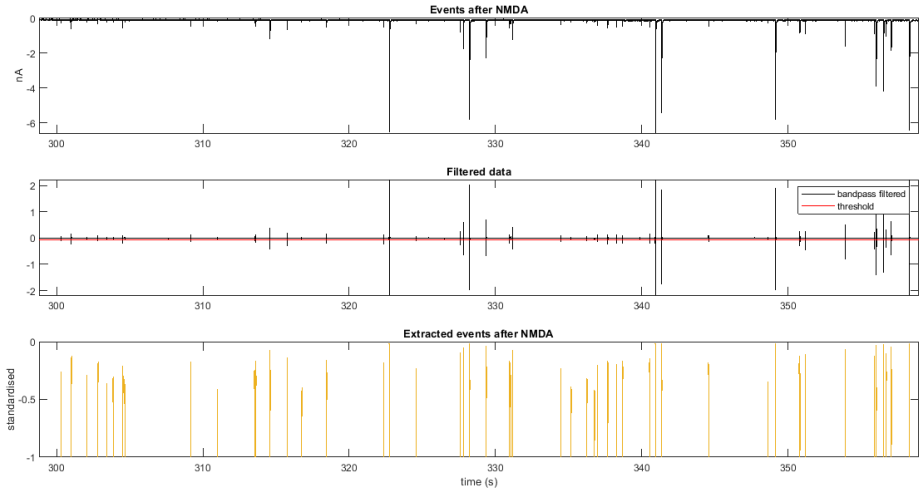

(a) 58 seconds

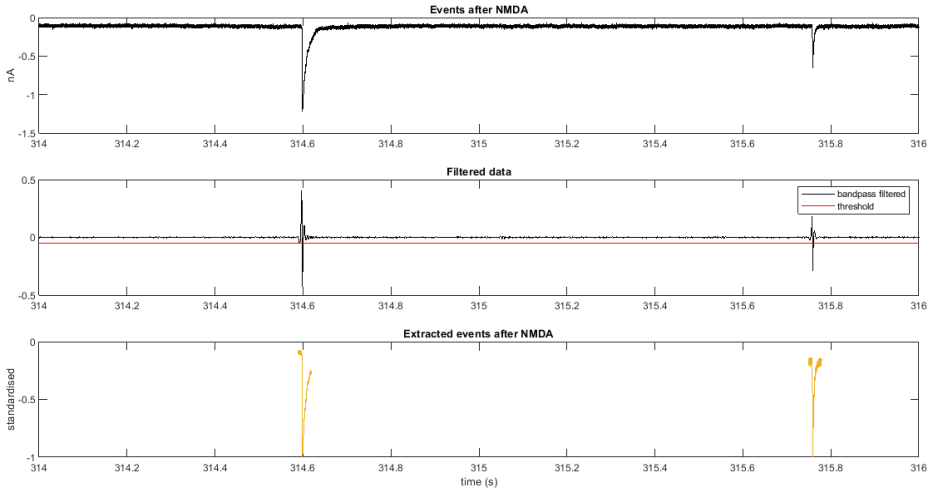

(b) Zoomin: 2 seconds

Figure 19: Threshold based event detection: (a) Events after NMDA: this shows ∼58 seconds of data after 10 uM NMDA was washed in at 298.75 seconds. Filtered data: bandpass filtered data (black) and event detection threshold (red) at -0.0351. There are 52 extracted events: each waveform (orange) is peak aligned, i.e. 100 data points before and after the peak (minimum amplitude). (b) Shows details of the some detected events that vary greatly in amplitude. Threshold = -0.05 (set by visual inspection).

	Pre NMDA Events							
	percent			count		Hz		seconds
file	μ slow	μ fast	σ	μ slow	μ fast	μ slow	μ fast	time window
N1.1	25.9	74.1	9.6	20.2	57.8	0.09	0.26	222.9
N1.2	27.2	72.8	11.4	21.2	56.8	0.10	0.25	222.9
N1.3	12.2	87.8	2.4	9.5	68.5	0.04	0.31	222.9
mean	21.8					0.08	0.27	

Table 24: Classification of pre NMDA events over 30 trials. On average, only about 21.8% were slow events. A neural network with 10 hidden nodes using the SCG training function was trained on known post DNQX and bicc events from file pairs (D1,B1), (D2,B2), (D3,B3); it classified the pre NMDA events in file N1 as N1.1, N1.2, N1.3 respectively. Event detection was by threshold versus filtered data: threshold = -0.05 (set by visual inspection). Detected 78 events.

	Post NMDA Events							
	percent			count		Hz		seconds
file	μ slow	μ fast	σ	μ slow	μ fast	μ slow	μ fast	time window
N1.1	40.5	59.5	5.4	20.6	30.4	0.36	0.52	58.0
N1.2	44.6	55.4	5.1	22.8	28.2	0.39	0.49	58.0
N1.3	31.3	68.7	1.5	16.0	35.0	0.28	0.60	58.0
mean	38.8					0.34	0.54	

Table 25: Classification of post NMDA events over 30 trials. On average, about 38.8% were slow events. A neural network with 10 hidden nodes using the SCG training function was trained on post DNQX and bicc events from file pairs (D1,B1), (D2,B2), (D3,B3); it classified the post NMDA events in file N1 as N1.1, N1.2, N1.3 respectively. Event detection was by threshold versus filtered data: = -0.05 (set by visual inspection). Detected 52 events.

5 Discussion

5.1 Neural network versus templates

Essentially, the NN methods were much easier to apply to the data and they provided better classification accuracy. While it was possible to tinker with various template parameters and occasionally get good results, that method was very sensitive to parameter settings. Also, the template method required time constants and a specific template length to build each template and several other parameter. But progress with neural networks was very fast. The NN selected features automatically by learning from examples; there was no need to annotate data with features by hand, or estimate the event time constants.

Automatic feature selection was also the reason why the SCG training function was chosen over the BR training function. Although the Bayesian regularisation training function (BR) had the highest classification accuracy when given four selected features,

data with such detailed annotations are not always available. It was possible to get ∼98% accuracy fast with SCG and without spending large amounts of time meticulously annotating data, so it made sense to parameterise the NN with SCG.

There is still the matter of fully automated event time detection, but given the right bandpass filter, it was quite easy to set the threshold such that nearly all events were detected. While templates can be less sensitive to the amplitude threshold for event detection, they don't solve the problem.

5.2 Pre versus post drug events

The NN classified 90.9% of pre DNQX events as slow events. In contrast, only about 50.8% of pre bicc events were classified as slow. While these averages are based on just three file pairs, the difference seems to indicate that the pre drug conditions were different in the DNQX experiments. It should be noted that event waveforms were extracted at ground truth detection times, and the NN was trained on the same set of examples for each pair of pre drug classifications.

5.3 Presynaptic NMDA receptors have been the subject of debate

Duguid and Smart [35] identified a new form of inhibitory synaptic plasticity called depolarization-induced potentiation of inhibition (DPI). Induction of DPI requires a rapid rise in postsynaptic Ca^{2+} in the PC, and release of glutamate (or a glutamate-like substance) that diffuses back to presynaptic NMDA receptors. Activation of the preNMDARs and release of Ca^{2+} from ryanodine-sensitive presynaptic stores were found to be sufficient to enhance GABAergic transmission [35].

However, preNMDARs have been surrounded by debate, mostly regarding their function and precise location [6, 33], and studies of axonal NMDARs in cerebellar molecular layer interneurons, consisting of basket cells and stellate cells, have produced conflicting results [84].

Some studies did not find evidence for axonal NMDARs [25, 26, 27]. For example, a search for preNMDAR mediated Ca^{2+} entry in cerebellar stellate cell axons did not reveal functional channels [25]. They found that NMDARs are expressed on dendrites, but not axons, and concluded that SC dendritic NMDAR activation masquerades as a presynaptic phenomenon [25]. However, the presence of preNMDARs depends on the age of the animal [6], and while other researchers used very young animals, Christie and Jahr used older Sprague Dawley rats (postnatal day 15–20) [25].

Later research by Pugh and Jahr in 2011 [84] used Sprague Dawley rats (postnatal day 8-18) to match those used in previous studies that found expression of presynaptic NMDARs in MLIs, but they still found no evidence of functional NMDARs in basket cell varicosities. Iontophoresis of the NMDAR agonist L-aspartate onto basket cell axon collaterals had no effect on evoked IPSCs measured in synaptically coupled Purkinje cells. In addition, calcium indicators in BC varicosities did not show any change in intracellular

calcium following application of L-aspartate or two-photon uncaging of glutamate [84].

In contrast, preNMDAR facilitation or modulation of release has been found by many labs: [18, 60], cerebellum [14, 35, 41, 42], cortex [10, 96], and hippocampus [73]. There is evidence that preNMDAR supralinearities are only found at a subset of boutons [19], this may help explain the apparently contradictory results.

In general, the preponderance of experimental evidence supports the existence of preNMDARs. But how can preNMDAR signalling in evoked and spontaneous release be differentially regulated [6]?

Abrahamsson et al [2] demonstrated that, at connected layer 5 pyramidal cell pairs of developing mouse visual cortex, Mg^{2+}-sensitive preNMDAR signalling upregulates replenishment of the readily releasable vesicle pool during high-frequency firing. Presynaptic NMDAR upregulation of vesicle replenishment was abolished in conditional RIM1$\alpha\beta$ deletion mice. And yet preNMDAR control of spontaneous release was unaffected. Looking at this in the opposite way, even though JNK2 blockade prevented Mg^{2+}-insensitive preNMDAR signalling from regulating spontaneous release, preNMDAR retained control of evoked release. So, Abrahamsson et al [2] showed that evoked and spontaneous release are controlled by independent and non-overlapping mechanisms. Presynaptic NMDARs may sometimes signal metabotropically; evoked and spontaneous release are distinct processes [2].

5.4 Presynaptic NMDA receptor location

The conflicting results circuitous explanations presented in the previous section provide an indication of the complex nature of synaptic interaction at Purkinje cells. While some mechanisms appear to work against each other, it seems likely that this combination of mechanisms supports the fine tuning and stability of synaptic strength. Nonetheless, preNMDARs are present.

Yet the preliminary results in this report are inconclusive with regard to preNMDAR locations. More analysis of the data recorded under experimental conditions, as summarised in Section 3.8, Tables 2 to 12, may lead to answers.

With regard to presynaptic NMDARs, only the pre and post drug events in the NMDA file "N1" was analysed. Those results indicate the presence of NMDA receptors, but not their exact locations.

In Section 4.2.5, Tables 24 and 25 show that 21.8% of events were classified as slow before NMDA, then increased to 38.8% after NMDA. And perhaps more importantly, the rate of slow events increased from 0.08 Hz to 0.34 Hz, while the rate of fast events only increased from 0.27 to 0.54 Hz. This suggests that NMDA strongly increased the activation of NMDARs on the presynaptic interneuron terminals, causing the release of more GABA, more activation of $GABA_A$ receptors on the PC soma, and more slow events.

While the increased rate of fast events was not as great, it was nonetheless a 100% increase. Apparently NMDA also activated NMDARs on the presynaptic climbing fibre terminals, causing the release of more glutamate, more activation of AMPA receptors on the PC soma, and more fast events.

However, there are at least two issues.

- Firstly, postsynaptic NMDA receptors are expressed in Purkinje cells of newborn animals and lost after postnatal day (P)12 [75], but the data in this report was recorded from newborn P(10) animals. Therefore, the application of NMDA to post synaptic NMDARs on the PC soma could have contributed to the increase in post synaptic current events. For example, the NN would classify NMDA currents as slow events after the post synaptic NMDARs were activated by NMDA and then glutamate form the climbing fibre terminals.

- Secondly, the synapses and structures that remained after vibrodissociation [54] are not known. It may be that more than just interneuron and climbing fibre presynaptic terminals remained, i.e. parts of the dendritic trees that could receive excitatory inputs. Consequently, if those structures remained, then those potential preNMDAR locations may have played a role.

6 Future Work

The threshold versus filtered data method for event detection worked well, but it could be refined especially with regard to filter construction and application. For example, a higher order Butterworth filter might improve detection by reducing ripples. The bandpass of cut-off frequencies should be optimised, but it was not obvious how to automatically map the time constant event features to the best bandpass range.

There remains an abundance of data recorded under specific pharmacological conditions that could be analysed with the support of methods presented in this report. For example, presynaptic glycine receptors may exist on climbing fibre boutons, and glycine may act as an excitatory transmitter in very young rodents (neonatal), but as an inhibitory transmitter in rodents more than about two weeks old. Therefore, the data relevant to presynaptic glycine receptors should be analysed.

7 Conclusion

Recordings from the soma of dissociated Purkinje cells contain an overlapping mixture of slow (gabaergic) and fast (glutamatergic) events with highly variable kinetics. While mixed events are difficult to classify, they trigger complex synaptic feedback interactions with the presynaptic terminals under physiological conditions that are lost when events of one type are blocked.

The primary aim of this report was to investigate whether or not neural networks are better than traditional template based methods for the classification of events with highly variable kinetics that may overlap in terms of shape and time, i.e. recorded before the application of blockers. Given accurate detection times for event extraction, the neural network based method parameterised with the scale conjugate gradient learning function was more accurate, more reliable, easier to apply than template based methods, and it

scales well to high dimensional data. For data that has been annotated with a small number of features, the Bayesian regularisation training function (BR) should be considered. Overall, neural network based methods are very flexible and well suited learning from the post synaptic event data in this report.

References

[1] M A Abdul-Ghani, T A Valiante, and P S Pennefather. Sr2+ and quantal events at excitatory synapses between mouse hippocampal neurons in culture. *The Journal of physiology*, 495 (Pt 1):113–125, August 1996.

[2] Therése Abrahamsson, Christina You Chien Chou, Si Ying Li, Adamo Mancino, Rui Ponte Costa, Jennifer Anne Brock, Erin Nuro, Katherine Anne Buchanan, Dale Elgar, Arne Vladimir Blackman, Adam Tudor-Jones, Julia Oyrer, William Todd Farmer, Keith Kazuo Murai, and Per Jesper Sjöström. Differential Regulation of Evoked and Spontaneous Release by Presynaptic NMDA Receptors. *Neuron*, 96:839–855.e5, November 2017.

[3] Norio Akaike and Andrew J Moorhouse. Techniques: applications of the nerve-bouton preparation in neuropharmacology. *Trends in pharmacological sciences*, 24:44–47, January 2003.

[4] N Ankri, P Legendre, D S Faber, and H Korn. Automatic detection of spontaneous synaptic responses in central neurons. *Journal of neuroscience methods*, 52:87–100, April 1994.

[5] Ariel Avila, Laurent Nguyen, and Jean-Michel Rigo. Glycine receptors and brain development. *Frontiers in cellular neuroscience*, 7:184, October 2013.

[6] Abhishek Banerjee, Rylan S Larsen, Benjamin D Philpot, and Ole Paulsen. Roles of Presynaptic NMDA Receptors in Neurotransmission and Plasticity. *Trends in neurosciences*, 39:26–39, January 2016.

[7] Scott Bardo, Michele G Cavazzini, and Nigel Emptage. The role of the endoplasmic reticulum Ca2+ store in the plasticity of central neurons. *Trends in pharmacological sciences*, 27:78–84, February 2006.

[8] Amor Belmeguenai, Eric Hosy, Fredrik Bengtsson, Christine M Pedroarena, Claire Piochon, Eva Teuling, Qionger He, Gen Ohtsuki, Marcel T G De Jeu, Ype Elgersma, Chris I De Zeeuw, Henrik Jörntell, and Christian Hansel. Intrinsic plasticity complements long-term potentiation in parallel fiber input gain control in cerebellar Purkinje cells. *The Journal of neuroscience : the official journal of the Society for Neuroscience*, 30:13630–13643, October 2010.

[9] H Bergman and M R DeLong. A personal computer-based spike detector and sorter: implementation and evaluation. *Journal of neuroscience methods*, 41:187–197, March 1992.

[10] N Berretta and R S Jones. Tonic facilitation of glutamate release by presynaptic N-methyl-D-aspartate autoreceptors in the entorhinal cortex. *Neuroscience*, 75:339–344, November 1996.

[11] Robert Bestel, Andreas W Daus, and Christiane Thielemann. A novel automated spike sorting algorithm with adaptable feature extraction. *Journal of neuroscience methods*, 211:168–178, October 2012.

[12] H Betz. Glycine receptors: heterogeneous and widespread in the mammalian brain. *Trends in neurosciences*, 14:458–461, October 1991.

[13] Giovanni Bianchi and Roberto Sorrentino. *Electronic filter simulation & design*. McGraw-Hill New York, 2007.

[14] Céline Bidoret, Annick Ayon, Boris Barbour, and Mariano Casado. Presynaptic NR2A-containing NMDA receptors implement a high-pass filter synaptic plasticity rule. *Proceedings of the National Academy of Sciences of the United States of America*, 106:14126–14131, August 2009.

[15] Céline Bidoret, Guy Bouvier, Annick Ayon, Germán Szapiro, and Mariano Casado. Properties and molecular identity of NMDA receptors at synaptic and non-synaptic inputs in cerebellar molecular layer interneurons. *Frontiers in synaptic neuroscience*, 7:1, 2015.

[16] ML Blanke and AMJ VanDongen. *Activation Mechanisms of the NMDA Receptor.*, volume Biology of the NMDA Receptor., chapter 13. CRC Press/Taylor & Francis, 2009.

[17] Ron Bouchard, Roberto Pattarini, and Jonathan D Geiger. Presence and functional significance of presynaptic ryanodine receptors. *Progress in neurobiology*, 69:391–418, April 2003.

[18] Daniel J Brasier and Daniel E Feldman. Synapse-specific expression of functional presynaptic NMDA receptors in rat somatosensory cortex. *The Journal of neuroscience : the official journal of the Society for Neuroscience*, 28:2199–2211, February 2008.

[19] Katherine A Buchanan, Arne V Blackman, Alexandre W Moreau, Dale Elgar, Rui P Costa, Txomin Lalanne, Adam A Tudor Jones, Julia Oyrer, and P Jesper Sjöström. Target-specific expression of presynaptic NMDA receptors in neocortical microcircuits. *Neuron*, 75:451–466, August 2012.

[20] Stephen Butterworth. On the theory of filter amplifiers. *Wireless Engineer*, 7(6):536–541, 1930.

[21] C G Carlson and J W Krieger. A baseline detection method for analyzing transient electrophysiological events. *Journal of neuroscience methods*, 67:211–220, August 1996.

[22] M Casado, S Dieudonné, and P Ascher. Presynaptic N-methyl-D-aspartate receptors at the parallel fiber-Purkinje cell synapse. *Proceedings of the National Academy of Sciences of the United States of America*, 97:11593–11597, October 2000.

[23] Mariano Casado, Philippe Isope, and Philippe Ascher. Involvement of presynaptic N-methyl-D-aspartate receptors in cerebellar long-term depression. *Neuron*, 33:123–130, January 2002.

[24] W L Caulfield, I T Collie, R S Dickins, O Epemolu, R McGuire, D R Hill, G McVey, J R Morphy, Z Rankovic, and H Sundaram. The first potent and selective inhibitors of the glycine transporter type 2. *Journal of medicinal chemistry*, 44:2679–2682, August 2001.

[25] Jason M Christie and Craig E Jahr. Dendritic NMDA receptors activate axonal calcium channels. *Neuron*, 60:298–307, October 2008.

[26] Jason M Christie and Craig E Jahr. Selective expression of ligand-gated ion channels in L5 pyramidal cell axons. *The Journal of neuroscience : the official journal of the Society for Neuroscience*, 29:11441–11450, September 2009.

[27] Beverley A Clark and Stuart G Cull-Candy. Activity-dependent recruitment of extrasynaptic NMDA receptor activation at an AMPA receptor-only synapse. *The Journal of neuroscience : the official journal of the Society for Neuroscience*, 22:4428–4436, June 2002.

[28] J D Clements and J M Bekkers. Detection of spontaneous synaptic events with an optimally scaled template. *Biophysical journal*, 73:220–229, July 1997.

[29] J H Cocatre-Zilgien and F Delcomyn. A slope-based approach to spike discrimination in digitized data. *Journal of neuroscience methods*, 33:241–249, August 1990.

[30] S L Cochran. Algorithms for detection and measurement of spontaneous events. *Journal of neuroscience methods*, 50:105–121, October 1993.

[31] Thibault Collin, Alain Marty, and Isabel Llano. Presynaptic calcium stores and synaptic transmission. *Current opinion in neurobiology*, 15:275–281, June 2005.

[32] DL Donoho and IM Johnstone. Ideal spatial adaptation by wavelet shrinkage. Biometrika 81 425–455. *Mathematical Reviews (MathSciNet): MR1311089 Zentralblatt MATH*, 815, 1994.

[33] Ian Duguid and Per Jesper Sjöström. Novel presynaptic mechanisms for coincidence detection in synaptic plasticity. *Current opinion in neurobiology*, 16:312–322, June 2006.

[34] Ian C Duguid, Yuriy Pankratov, Guy W J Moss, and Trevor G Smart. Somatodendritic release of glutamate regulates synaptic inhibition in cerebellar Purkinje cells via autocrine mGluR1 activation. *The Journal of neuroscience : the official journal of the Society for Neuroscience*, 27:12464–12474, November 2007.

[35] Ian C Duguid and Trevor G Smart. Retrograde activation of presynaptic NMDA receptors enhances GABA release at cerebellar interneuron-Purkinje cell synapses. *Nature neuroscience*, 7:525–533, May 2004.

[36] Smart TG. Duguid IC. *Presynaptic NMDA Receptors.*, volume Biology of the NMDA Receptor., chapter 14. CRC Press/Taylor & Francis, 2009.

[37] J C Eccles, R Llinás, and K Sasaki. The excitatory synaptic action of climbing fibres on the Purkinje cells of the cerebellum. *The Journal of physiology*, 182:268–296, January 1966.

[38] J C Eccles, R Llinás, K Sasaki, and P E Voorhoeve. Interaction experiments on the responses evoked in Purkinje cells by climbing fibres. *The Journal of physiology*, 182:297–315, January 1966.

[39] G.B. Ermentrout and D.H. Terman. *Mathematical Foundations of Neuroscience*. Springer, 2010.

[40] Zhenyu Gao, Boeke J van Beugen, and Chris I De Zeeuw. Distributed synergistic plasticity and cerebellar learning. *Nature reviews. Neuroscience*, 13:619–635, September 2012.

[41] M Glitsch and A Marty. Presynaptic effects of NMDA in cerebellar Purkinje cells and interneurons. *The Journal of neuroscience : the official journal of the Society for Neuroscience*, 19:511–519, January 1999.

[42] M D Glitsch. Calcium influx through N-methyl-D-aspartate receptors triggers GABA release at interneuron-Purkinje cell synapse in rat cerebellum. *Neuroscience*, 151:403–409, January 2008.

[43] C M Gray, P E Maldonado, M Wilson, and B McNaughton. Tetrodes markedly improve the reliability and yield of multiple single-unit isolation from multi-unit recordings in cat striate cortex. *Journal of neuroscience methods*, 63:43–54, December 1995.

[44] Segundo J Guzman, Alois Schlögl, and Christoph Schmidt-Hieber. Stimfit: quantifying electrophysiological data with Python. *Frontiers in neuroinformatics*, 8:16, 2014.

[45] Martin T Hagan and Mohammad B Menhaj. Training feedforward networks with the Marquardt algorithm. *IEEE transactions on Neural Networks*, 5(6):989–993, 1994.

[46] M.T. Hagan, H.B. Demuth, and M.H. Beale. *Neural Network Design*. Boston, MA: PWS Publishing, 1996.

[47] David J. Hand, Padhraic Smyth, and Heikki Mannila. *Principles of Data Minin*. MIT Press, Cambridge, MA, USA, 2001.

[48] Catriona M Houston, Damian P Bright, Lucia G Sivilotti, Marco Beato, and Trevor G Smart. Intracellular chloride ions regulate the time course of GABA-mediated inhibitory synaptic transmission. *The Journal of neuroscience : the official journal of the Society for Neuroscience*, 29:10416–10423, August 2009.

[49] T N Hwang and D R Copenhagen. Automatic detection, characterization, and discrimination of kinetically distinct spontaneous synaptic events. *Journal of neuroscience methods*, 92:65–73, October 1999.

[50] M Ito. Cerebellar long-term depression: characterization, signal transduction, and functional roles. *Physiological reviews*, 81:1143–1195, July 2001.

[51] M Ito and M Kano. Long-lasting depression of parallel fiber-Purkinje cell transmission induced by conjunctive stimulation of parallel fibers and climbing fibers in the cerebellar cortex. *Neuroscience letters*, 33:253–258, December 1982.

[52] Susumu Ito. GABA and glycine in the developing brain. *The journal of physiological sciences : JPS*, 66:375–379, September 2016.

[53] P Jonas, G Major, and B Sakmann. Quantal components of unitary EPSCs at the mossy fibre synapse on CA3 pyramidal cells of rat hippocampus. *The Journal of physiology*, 472:615–663, December 1993.

[54] Sang Beom Jun, Verginia Cuzon Carlson, Stephen Ikeda, and David Lovinger. Vibrodissociation of neurons from rodent brain slices to study synaptic transmission and image presynaptic terminals. *Journal of visualized experiments : JoVE*, May 2011.

[55] Kazuyoshi Kawa. Glycine facilitates transmitter release at developing synapses: a patch clamp study from Purkinje neurons of the newborn rat. *Brain research. Developmental brain research*, 144:57–71, August 2003.

[56] Sunghwan Kim, Jie Chen, Tiejun Cheng, Asta Gindulyte, Jia He, Siqian He, Qingliang Li, Benjamin A Shoemaker, Paul A Thiessen, Bo Yu, Leonid Zaslavsky, Jian Zhang, and Evan E Bolton. PubChem 2019 update: improved access to chemical data. *Nucleic acids research*, 47:D1102–D1109, January 2019.

[57] I C Kleppe and H P Robinson. Determining the activation time course of synaptic AMPA receptors from openings of colocalized NMDA receptors. *Biophysical journal*, 77:1418–1427, September 1999.

[58] Kevin J. Lang, Alex H. Waibel, and Geoffrey E. Hinton. A time-delay neural network architecture for isolated word recognition. *Neural Networks*, 3(1):23 – 43, 1990.

[59] Salomon Z Langer. Presynaptic autoreceptors regulating transmitter release. *Neurochemistry international*, 52:26–30, January 2008.

[60] Rylan S Larsen, Rebekah J Corlew, Maile A Henson, Adam C Roberts, Masayoshi Mishina, Masahiko Watanabe, Stuart A Lipton, Nobuki Nakanishi, Isabel Pérez-Otaño, Richard J Weinberg, and Benjamin D Philpot. NR3A-containing NMDARs promote neurotransmitter release and spike timing-dependent plasticity. *Nature neuroscience*, 14:338–344, March 2011.

[61] Y. LeCun, B. Boser, J. S. Denker, D. Henderson, R. E. Howard, W. Hubbard, and L. D. Jackel. Backpropagation Applied to Handwritten Zip Code Recognition. *Neural Computation*, 1(4):541–551, December 1989.

[62] Yann LeCun, Yoshua Bengio, and Geoffrey Hinton. Deep learning. *Nature*, 521:436–444, May 2015.

[63] Varda Lev-Ram, Scott T Wong, Daniel R Storm, and Roger Y Tsien. A new form of cerebellar long-term potentiation is postsynaptic and depends on nitric oxide but not cAMP. *Proceedings of the National Academy of Sciences of the United States of America*, 99:8389–8393, June 2002.

[64] C Levenes, H Daniel, and F Crepel. Retrograde modulation of transmitter release by postsynaptic subtype 1 metabotropic glutamate receptors in the rat cerebellum. *The Journal of physiology*, 537:125–140, November 2001.

[65] M S Lewicki. A review of methods for spike sorting: the detection and classification of neural action potentials. *Network (Bristol, England)*, 9:R53–R78, November 1998.

[66] D Liao, A Jones, and R Malinow. Direct measurement of quantal changes underlying long-term potentiation in CA1 hippocampus. *Neuron*, 9:1089–1097, December 1992.

[67] H H Liu and Y I Kim. A computer system for real-time data acquisition and analysis of biopotentials and quantal content at the neuromuscular junction. *Computer programs in biomedicine*, 16:161–173, June 1983.

[68] Rodolfo Llinas and Mario N Negrello. Cerebellum. *Scholarpedia*, 10(1):4606, 2015.

[69] Yonatan Loewenstein, Séverine Mahon, Paul Chadderton, Kazuo Kitamura, Haim Sompolinsky, Yosef Yarom, and Michael Häusser. Bistability of cerebellar Purkinje cells modulated by sensory stimulation. *Nature neuroscience*, 8:202–211, February 2005.

[70] Mike Ludwig and Quentin J Pittman. Talking back: dendritic neurotransmitter release. *Trends in neurosciences*, 26:255–261, May 2003.

[71] Donald W Marquardt. An algorithm for least-squares estimation of nonlinear parameters. *Journal of the society for Industrial and Applied Mathematics*, 11(2):431–441, 1963.

[72] The Mathworks, Inc., Natick, Massachusetts. *Deep Learning Toolbox*, 2019.

[73] Lindsay McGuinness, Chanel Taylor, Ruth D T Taylor, Christopher Yau, Tobias Langenhan, Michael L Hart, Helen Christian, Patricia W Tynan, Peter Donnelly, and Nigel J Emptage. Presynaptic NMDARs in the hippocampus facilitate transmitter release at theta frequency. *Neuron*, 68:1109–1127, December 2010.

[74] Thomas M. Mitchell. *Machine Learning*. McGraw-Hill, Inc., New York, NY, USA, 1 edition, 1997.

[75] A Momiyama, D Feldmeyer, and S G Cull-Candy. Identification of a native low-conductance NMDA channel with reduced sensitivity to Mg2+ in rat central neurones. *The Journal of physiology*, 494 (Pt 2):479–492, July 1996.

[76] F R Morales, P A Boxer, J P Jervey, and M H Chase. A computerized system for the detection and analysis of spontaneously occurring synaptic potentials. *Journal of neuroscience methods*, 13:19–35, March 1985.

[77] J S Oghalai, W N Street, and W S Rhode. A neural network-based spike discriminator. *Journal of neuroscience methods*, 54:9–22, September 1994.

[78] Gen Ohtsuki, Claire Piochon, and Christian Hansel. Climbing fiber signaling and cerebellar gain control. *Frontiers in cellular neuroscience*, 3:4, 2009.

[79] Alan V Oppenheim. *Discrete-time signal processing*. Pearson Education India, 1999.

[80] Sanford L Palay and Victoria Chan-Palay. *Cerebellar cortex: cytology and organization*. Springer, 1974.

[81] Alejandro Javier Pernía-Andrade, Sarit Pati Goswami, Yvonne Stickler, Ulrich Fröbe, Alois Schlögl, and Peter Jonas. A deconvolution-based method with high sensitivity and temporal resolution for detection of spontaneous synaptic currents in vitro and in vivo. *Biophysical journal*, 103:1429–1439, October 2012.

[82] Claire Piochon, Theano Irinopoulou, Daniel Brusciano, Yannick Bailly, Jean Mariani, and Carole Levenes. NMDA receptor contribution to the climbing fiber response in the adult mouse Purkinje cell. *The Journal of neuroscience : the official journal of the Society for Neuroscience*, 27:10797–10809, October 2007.

[83] D S Poskitt, K Dogançay, and S H Chung. A new analytical method of studying post-synaptic currents. *Mathematical biosciences*, 161:15–41, October 1999.

[84] Jason R Pugh and Craig E Jahr. NMDA receptor agonists fail to alter release from cerebellar basket cells. *The Journal of neuroscience : the official journal of the Society for Neuroscience*, 31:16550–16555, November 2011.

[85] R Quian Quiroga, Zoltan Nadasdy, and Yoram Ben-Shaul. Unsupervised spike detection and sorting with wavelets and superparamagnetic clustering. *Neural computation*, 16(8):1661–1687, 2004.

[86] Rodrigo Quian Quiroga. Spike sorting. *Scholarpedia*, 2(12):3583, 2007.

[87] I M Raman and B P Bean. Ionic currents underlying spontaneous action potentials in isolated cerebellar Purkinje neurons. *The Journal of neuroscience : the official journal of the Society for Neuroscience*, 19:1663–1674, March 1999.

[88] Massimiliano Renzi, Mark Farrant, and Stuart G Cull-Candy. Climbing-fibre activation of NMDA receptors in Purkinje cells of adult mice. *The Journal of physiology*, 585:91–101, November 2007.

[89] Hernan Gonzalo Rey, Carlos Pedreira, and Rodrigo Quian Quiroga. Past, present and future of spike sorting techniques. *Brain research bulletin*, 119:106–117, 2015.

[90] David E. Rumelhart, Bernard Widrow, and Michael A. Lehr. The Basic Ideas in Neural Networks. *Commun. ACM*, 37(3):87–92, March 1994.

[91] M Salganicoff, M Sarna, L Sax, and G L Gerstein. Unsupervised waveform classification for multi-neuron recordings: a real-time, software-based system. I. Algorithms and implementation. *Journal of neuroscience methods*, 25:181–187, October 1988.

[92] P A Salin, R C Malenka, and R A Nicoll. Cyclic AMP mediates a presynaptic form of LTP at cerebellar parallel fiber synapses. *Neuron*, 16:797–803, April 1996.

[93] Eric De Schutter, editor. *Computational modeling method for neuroscientists*, chapter Chapter 6: Modeling Synapses, pages 139–159. The MIT Press, 2010.

[94] Yulin Shi, Zoran Nenadic, and Xiangmin Xu. Novel use of matched filtering for synaptic event detection and extraction. *PloS one*, 5:e15517, November 2010.

[95] Jung Hoon Shin and David J Linden. An NMDA receptor/nitric oxide cascade is involved in cerebellar LTD but is not localized to the parallel fiber terminal. *Journal of neurophysiology*, 94(6):4281–4289, 2005.

[96] Per Jesper Sjöström, Gina G Turrigiano, and Sacha B Nelson. Neocortical LTD via coincident activation of presynaptic NMDA and cannabinoid receptors. *Neuron*, 39:641–654, August 2003.

[97] David Sterratt, Bruce Graham, Andrew Gillies, and David Willshaw. *Principles of Computational Modelling in Neuroscience*. Cambridge University Press, 2011.

[98] David S. Touretzky, Jeffrey L. Elman, Terrence J. Sejnowski, and Geoffrey E. Hinton, editors. *Extracting features from faces using compression networks: Face, identity, emotion, and gender recognition using holons*, volume Proceedings of the 1990 Connectionist Models Summer School, University of California at San Diego, 1990.

[99] Stephen F Traynelis, Lonnie P Wollmuth, Chris J McBain, Frank S Menniti, Katie M Vance, Kevin K Ogden, Kasper B Hansen, Hongjie Yuan, Scott J Myers, and Ray Dingledine. Glutamate receptor ion channels: structure, regulation, and function. *Pharmacological reviews*, 62:405–496, September 2010.

[100] T Tyrrell and D Willshaw. Cerebellar cortex: its simulation and the relevance of Marr's theory. *Philosophical transactions of the Royal Society of London. Series B, Biological sciences*, 336:239–257, May 1992.

[101] Marylka Yoe Uusisaari and Thomas Knöpfel. Diversity of neuronal elements and circuitry in the cerebellar nuclei. *Cerebellum (London, England)*, 11:420–421, June 2012.

[102] Carmen Vidaurre, Tilmann H Sander, and Alois Schlögl. BioSig: the free and open source software library for biomedical signal processing. *Computational intelligence and neuroscience*, 2011:935364, 2011.

[103] V S Vorobjev. Vibrodissociation of sliced mammalian nervous tissue. *Journal of neuroscience methods*, 38:145–150, July 1991.

[104] J I Wadiche and C E Jahr. Multivesicular release at climbing fiber-Purkinje cell synapses. *Neuron*, 32:301–313, October 2001.

[105] S Yamada, H Kage, M Nakashima, S Shiono, and M Maeda. Data processing for multi-channel optical recording: action potential detection by neural network. *Journal of neuroscience methods*, 43:23–33, June 1992.

[106] X W Yang and S A Shamma. A totally automated system for the detection and classification of neural spikes. *IEEE transactions on bio-medical engineering*, 35:806–816, October 1988.

[107] Michael M Yartsev, Ronit Givon-Mayo, Michael Maller, and Opher Donchin. Pausing purkinje cells in the cerebellum of the awake cat. *Frontiers in systems neuroscience*, 3:2, 2009.

[108] Jiang-Hong Ye. Regulation of excitation by glycine receptors. *Results and problems in cell differentiation*, 44:123–143, 2008.

[109] Y Zilberter. Dendritic release of glutamate suppresses synaptic inhibition of pyramidal neurons in rat neocortex. *The Journal of physiology*, 528:489–496, November 2000.

8 Appendix

8.1 Synaptic plasticity in the cerebellum

Ito *et al.* [51] were the first to present experimental evidence for LTD induction at the parallel fibre–Purkinje cell synapse. Subsequently, LTD at the parallel fibre–Purkinje cell synapse was proposed to be the dominant type of plasticity for cerebellar learning [50]. However, there are many forms of plasticity, and they can occur at multiple synaptic and extrasynaptic sites and provide complementary or overlapping functions within the same network [40]. For example, procedural memory formation is mediated by various forms of plasticity to support movement coordination [8, 51, 63, 92], and repetitive firing of PFs alone can cause LTP [40].

PCs have two typical modes of firing: (1) PFs to PCs cause simple spikes. Purkinje cells receive their input from granule cells via thousands of parallel fibre varicosities [80]. All four forms of long-term plasticity (pre- and postsynaptic LTP/LTD) have been shown to occur at this synapse [40]. (2) CFs to PCs cause complex spikes. Simultaneous activation of hundreds of synapses can trigger complex spikes followed by quiet period [78].

CF–PC firing results in complex spikes in PCs. Some regard complex spikes as error signals for training the PF–PC synapse, results in LTD that weakens the guilty PF–PC synapses. Others regard climbing fibres as timing signals related to the onset of movement.

1. Simple spikes occur at rates of 17-150 Hz [87]. They can be spontaneous, or activated synaptically via parallel fibres (axons) from granule cells.

2. Complex spikes are slow, 1-3 Hz spikes. They are characterized by an initial prolonged large-amplitude spike, followed by a high-frequency burst of smaller-amplitude action potentials. They are caused by climbing fibre activation. Activation of the Purkinje cell by climbing fibres can shift its activity from a quiet state to a spontaneously active state and vice versa, like a toggle switch [69]; this activity has been observed in awake cats [107].

Both types of molecular layer interneuron (stellate cells and basket cells) are innervated by PFs [80]. Stellate cells inhibit Purkinje cell dendrites, whereas basket cells provide inhibition to the Purkinje cell soma [80].

8.2 Vibrodissociation of Neurons

The real data analysed in this report was recorded from vibration dissociated soma of Purkinje cells. Mechanical dissociation leaves presynaptic boutons attached to the cell of interest and, therefore, facilitates the examination of synaptic transmission while the extracellular and postsynaptic intracellular environments are controlled. Vibrodissociation provides many advantages over other methods such as cell cultures, brain slices and enzymatically isolated neurons [54].

8.3 Excitatory and Inhibitory Transmitters

The main excitatory and inhibitory transmitters in the CNS are glutamate and gamma-aminobutyric acid (GABA) respectively. In general, when glutamate binds to the postsynaptic receptor, positive ions such as Na^+ and K^+ rush in. The resulting depolarization causes an EPSP and makes the postsynaptic cell more likely to fire an action potential. In contrast, when GABA binds to the postsynaptic receptor, Cl^- ions rush in. The resulting hyper-polarisation causes an IPSP and makes the postsynaptic cell less likely to fire an action potential.

However, the reversal potential of some GABA receptors V_{GABA} is mostly dependent on [Cl^-], so V_{GABA} can be close to rest and even above the resting potential. Some GABA synapses can actually be excitatory, especially during early development. As is the case for other currents, this synaptic current can be modelled as the product of conductance times driving force (the voltage difference across the membrane) [39]

$$I_{syn} = g(t)(V_{post} - V_{GABA}). \tag{12}$$

where conductance at time $g(t)$ depends on the concentration of GABA in the synaptic cleft.

$GABA_A$ receptors are ionotropic and provide fast synaptic inhibition. A single presynaptic spike can trigger the release of GABA that binds to the $GABA_A$ receptors [39].

V_{GABA_A} varies between -81 and -60 mV. GABA current is primarily carried by chloride ions. Early in development GABA is usually depolarizing with V_{GABA} greater than rest [39].

Extracellular [Cl^-] is much greater than intracellular [Cl^-], about 120 mM versus 5 mM.

Nernst equation:

$$E_{Cl} = \frac{RT}{zF} \ln \frac{[Cl^-]_i}{[Cl^-]_o} \tag{13}$$

$$E_{Cl} = 61.5 \log_{10} \frac{5}{120} \approx -85mV \tag{14}$$

8.4 Presynaptic NMDARs as autoreceptors

Given the a lack of functional NMDARs on Purkinje cells [82, 88], LTD may be mediated as follows: repetitive parallel fibre activation triggers autoreceptor activation of presynaptic NMDARs expressed at parallel fibre axon terminals to initiate a signalling cascade leading to LTD [22, 23].

However, according to Shin and Linden [95], the NMDAR-NO cascade involved in cerebellar LTD is not localized to parallel fibres, but to inter-neuronal axon terminals [95]. The presynaptic NMDARs are most likely activated by glutamate spillover from the PFs, leading to NO (nitric oxide) release from interneurons. That NO diffuses to the Purkinje cells to evoke LTD. The correct explanation is not clear due to the lack of detailed EM immunostaining for NMDAR subunits on nerve terminals in the cerebellum [36].

The distribution of presynaptic NMDARs on asymmetrical synapses is widespread. This suggests that autoreceptor regulation of synaptic transmission is a prevalent feature of information processing throughout the mammalian CNS [36].

8.5 Bi-exponential functions

```
%%
% bi_exponential_1() standardises amplitude to 1,
% scales it to the desired amplitude with a, and
% returns a vector.
%
% t:  vector of time points
% max_amp:  amplitude (a small negative value in this project)
% t1:       rise time constant in time steps
% t2:       decay time constant in time steps
%
function y=bi_exponential_1(t, a, t1, t2)

y = (1 - exp(-t/t1)) * exp(-t/t2) );
y = a * (y./max(y));

end


%%
% Rising phase for this function is about 1.6 ms slower to
% peak than bi_exponential_1() when using time constants
% $\tau_1$=5 ms and $\tau_2$=25 ms
%
function y=bi_exponential_2(t, max_amp, t1, t2)

t3= (t1*t2)/(t2-t1);
y = ( exp(-t/t2) - exp(-t/t3) );
y = max_amp * (y./max(y));

end
```

Figure 20: Matlab definitions of bi-exponential functions.

8.6 Dual exponential function

The mean post synaptic waveform current for an event type can also be modelled with a so-called dual exponential function [97, p174], which is similar to the bi-exponential functions discussed in the report.

```
%%
% dual_exponential() standardises amplitude to 1,
% scales it to the desired amplitude with max_amp, and
% returns a vector.
%
% t:      vector of time points
% max_amp:  amplitude (a small negative value in this project)
% t1:       rise time constant in time steps
% t2:       decay time constant in time steps
%
function y = dual_exponential(t, max_amp, t1, t2)

% Note: for standardisation use y=y./max(y).

y=(t1*t2)*(exp(-t/t2)-exp(-t/t1))/(t2-t1);

y= y/max(y);
y= max_amp * y;

end
```

Figure 21: Matlab definition of a dual exponential function.

8.6.1 Script for generating synthetic data

```
%% set parameters for slow events and fast events
%
tau_r_slow  =  5  * rate;  % slow: rise time constant, rate converts ms to steps
tau_d_s_base= 15 * rate;   % slow: decay time constant base

tau_r_fast   = 0.5 * rate;  % fast:  rise time constant
tau_d_f_base = 1.5 * rate;  % fast:  decay time constant base

max_amp_slow=-1;     amp_sd_s=0.20;  % slow: max amplitude and std
max_amp_fast=-0.10;  amp_sd_f=0.10;  % fast: max amplitude and std

poisson_lambda_1=15000;  poisson_lambda_2=4000; % mean arrival times for poisson dist'd events

randn_IEI_1=3000;        randn_IEI_2=2000;      % mean intervals between normally dist'd events

%% generate events using poisson, normal, uniform, and exponentially distributed numbers.
for ii=1:100

    if rand < 0.2
        ts1=ts1 + 10 + poissrnd( poisson_lambda_1 );      % time of slow event burst
    end
    ts1=ts1 + round(abs(randn * randn_IEI_1));            % add inter event interval

    if rand < 0.2
        ts2=ts2 + poissrnd( poisson_lambda_2 );           % time of fast event burst
    end
    ts2=ts2 + round(abs(randn * randn_IEI_2));            % add inter event interval

    if ts1 >= tmax-1 && ts2 >= tmax-1                     % if done, break out of loop
        break;
    end

    tau_d_slow = tau_d_s_base + exprnd(tau_d_s_base);    % add exponentially distributed amount
                                                         % to slow decay time constant
    tau_d_fast = tau_d_f_base + exprnd(tau_d_f_base*3);  % add exponentially distributed amount
                                                         % to fast decay time constant

    %% the second part of the for loop is shown in the next figure.
```

Figure 22: Matlab script for generating synthetic data, part 1:

```
%% for loop continued
%  This is the second part of the for loop.

% t is all time points for event train
% ts1 is start time of event type 1 (slow event)
% ts2 is start time of event type 2 (fast event)
tr1=t(round(ts1/dt):length(t))-(ts1-dt);  % tr1=time window random 1 (slow event)
tr2=t(round(ts2/dt):length(t))-(ts2-dt);  % tr2=time window random 2 (fast event)

    %% make a new slow event using a parameterised dual exponential function
    % and add it to the slow event train
    if ts1 < tmax-1

        max_amp = max_amp_slow + ( amp_sd_s * randn);
        if max_amp > -0.10
            max_amp= -0.10;
        end
        new_wave = bi_exponential(tr1, max_amp, tau_r_slow, tau_d_slow);

        [~,idx]  = min(new_wave);
        wave_type(ts1+idx-1)=1;    % record ground truth, this is a fast event (type 2)
                                   % next, add new wave to event train

        psc_1(round(ts1/dt):length(t)) = psc_1(round(ts1/dt):length(t)) + new_wave;
    end

    %% make a new fast event using a parameterised dual exponential function
    %  and add it to the fast event train
    if ts2 < tmax-1

        max_amp = max_amp_f - exprnd(0.3);  % add exponentially distributed value to amplitude

        if max_amp > -0.05
            max_amp= -0.05;
        end

        new_wave = bi_exponential(tr2, max_amp, tau_r_fast, tau_d_fast);  % make waveform
        [~,idx]  = min(new_wave);

        wave_type(ts2+idx-1)=2;    % record ground truth, this is a fast event (type 2)
                                   % next, add new wave to event train

        psc_2(round(ts2/dt):length(t)) = psc_2(round(ts2/dt):length(t)) + new_wave;
    end
end
```

Figure 23: Matlab script for synthetic data, part 2.

8.7 Deconvolution

```
%% use FFT to transform into frequency domain
H = fft(template, size(r,1))
R = fft(r)

%% compute deconvolution in frequency domain
D = R./H;

%% bandpass filter [0.1,  150] in frequency domain
D = filter(D)

%% convert from frequency domain into time domain.
d = real(ifft(D));
```

Figure 24: Pseudo for the signal deconvolution function used in [81] where `r` is the data to be deconvolved.

8.8 Template method event detection and classification of the sum of real data

The following mixed event trains are the sum of real slow and fast event data. Slow event data is from DNQX-2, file "09921004.abf", at 40 to 90 seconds, fast event data is from bicc-2, file "16728001 v3.abf", at 250 to 300 seconds. The two were added together to create 50 seconds of mixed event data, as shown in Figure 25.

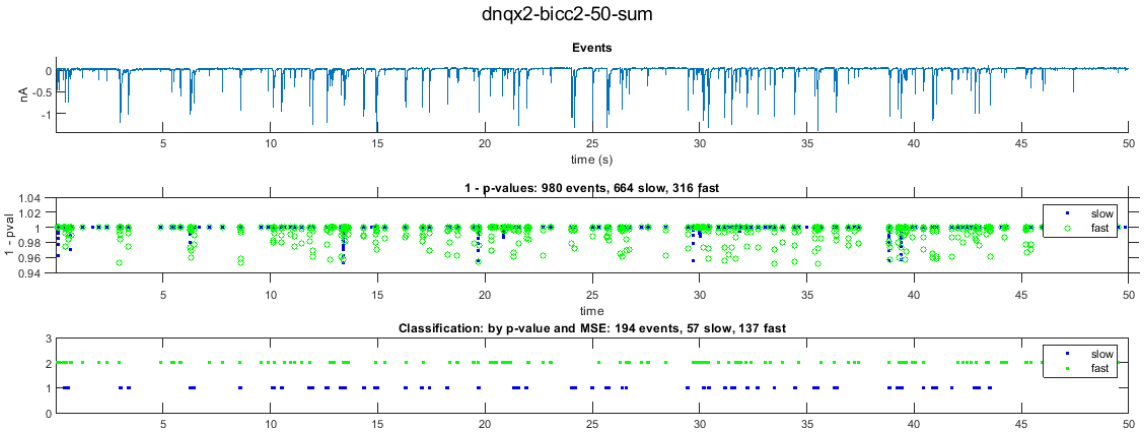

Figure 25: Real data: sum of DNQX-2 and bicc-2 data. This figure shows 50 seconds of mixed event data.

data	time (s)	event	count	percent	Hz
DNQX-2 + bicc-2	50	slow	57	29.4	1.14
DNQX-2 + bicc-2	50	fast	137	70.6	2.74

Table 26: Rates for TCE method: event detection and classification of real data, i.e. the sum of DNQX-2 and bicc-2 data. A total of 194 events were detected.

8.9 Deconvolution method on real data

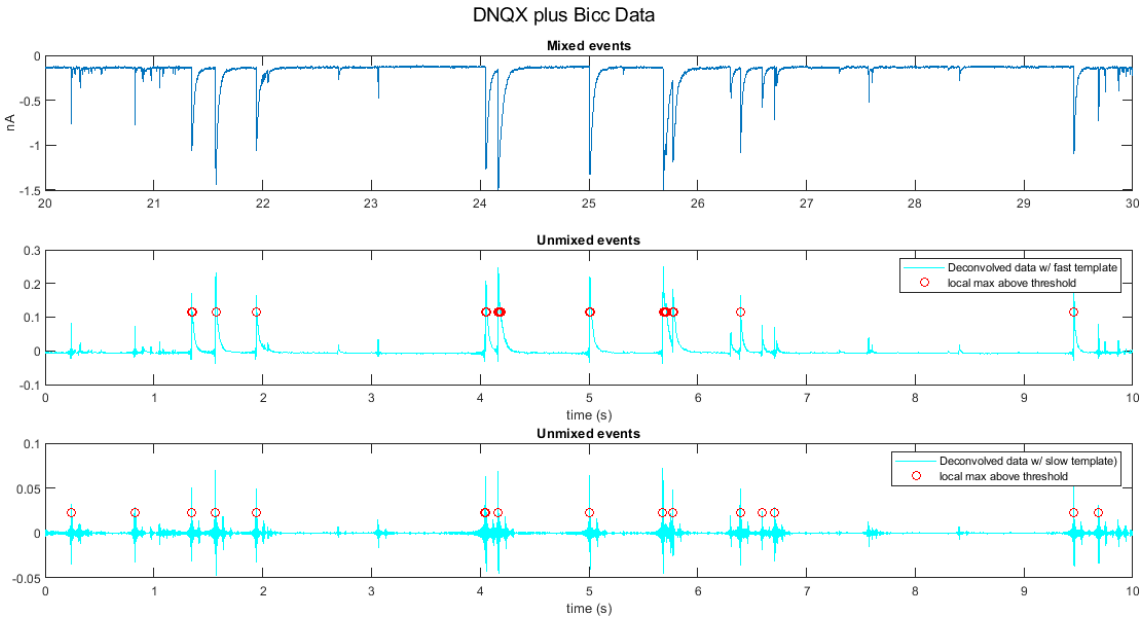

Figure 26: Real data: sum of DNQX-2 and bicc-2. This figure shows 10 seconds of mixed data, and the results from deconvolution with a fast template, and a slow template.

data	time (s)	event	count	percent	Hz
DNQX-2 + bicc-2	10	slow	9	-	-
DNQX-2 + bicc-2	10	fast	5	-	-

Table 27: Deconvolution method: event detection and classification of event trains composed of the sum of slow and fast events from DNQX-2 and bicc-2, extracted from files "09921004.abf" and "16728001 v3.abf" respectively. This method does not really classify events. Deconvolution with the slow template revealed both event types.

8.10 Neural network with 30 hidden nodes

This neural network had 1 hidden layer with 30 nodes and was tested with three training functions on the post drug data, the four file pairs (D1,B1) to (D4,B4). For this data, increasing the number of hidden nodes from 10 to 30 did not improve classification accuracy.

	Files D1, B1		Files D2, B2		Files D3, B3		Files D4, B4		All Files	
function	μ (%)	σ	μ (%)	σ	μ (%)	σ	μ (%)	σ	μ (%)	σ
SCG	92.77	3.35	77.39	10.41	98.98	0.29	94.96	1.17	91.03	3.81
LM	95.38	1.61	83.92	9.38	97.70	7.71	96.74	0.65	93.44	4.84
BR	96.77	0.87	94.90	2.18	99.20	0.47	96.88	10.48	**96.94**	3.50

Table 28: Accuracy of a neural network with 30 hidden nodes using three training functions over 30 trials on four pairs of data files. Bayesian regularization (BR) had the best mean accuracy over all files, but its runtime was about 200 seconds versus about 10 seconds for scaled conjugate gradient (SCG) and Levenberg-Marquardt (LM).

8.11 Neural network with 10 hidden nodes on waveforms extracted at ground truth detection times

The figures in Sections 8.11.1, 8.11.2, and 8.11.3 show results for one trial using a 10 node hidden layer NN with the SCG training function. Here, instead of 4 hand annotated features from the Excel files, the entire waveform for each event was extracted automatically from the unfiltered data and given as input to the NN, so the NN learned from examples with 201 features, all data points in each waveform.

8.11.1 Neural network results for file set 1

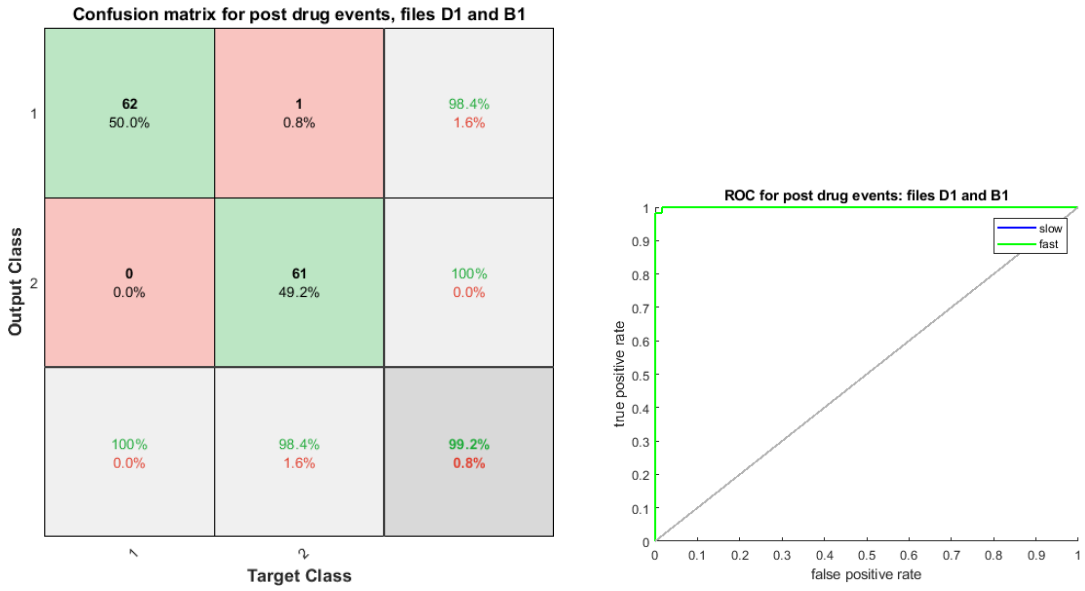

Figure 27: NN classification of post drug events: (a) confusion matrix shows an overall accuracy of 99.2%, (b) ROC curves. Data files D1 and B1.

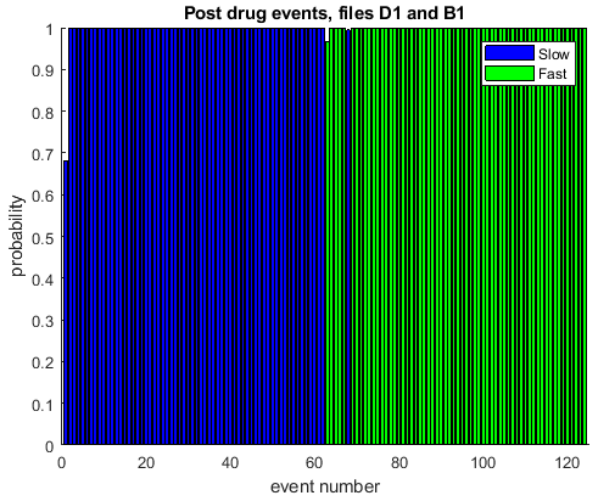

Figure 28: NN classification of post drug events: events 1 to 62 should be blue (slow), events 63 to 124 should be green (fast). Data files D1 and B1.

8.11.2 Neural network results for file set 2

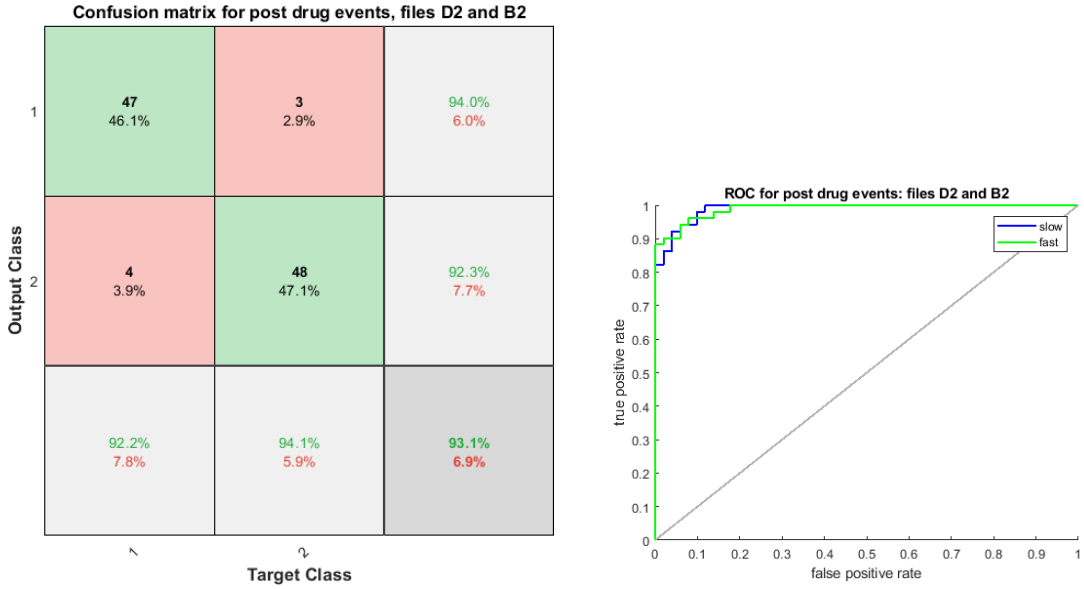

Figure 29: NN classification of post drug events: (a) confusion matrix: overall accuracy shown in bottom right was 93.1% (b) ROC curves. Data files D2 and B2.

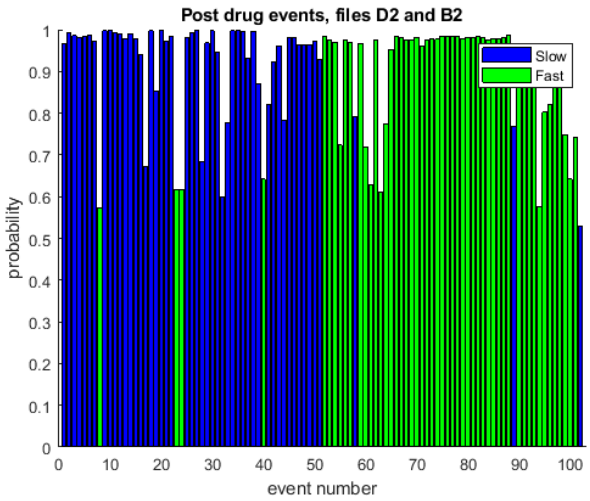

Figure 30: NN classification of post drug events: events 1 to 51 should be blue (slow), events 52 to 102 should be green (fast). Data files D2 and B2.

8.11.3 Neural network results for file set 3

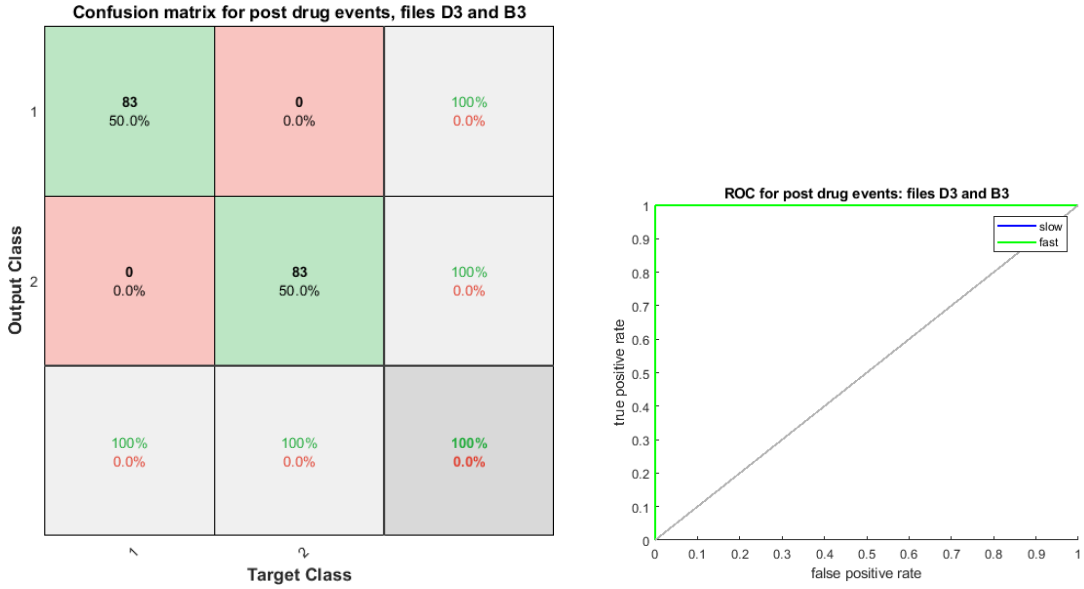

Figure 31: NN classification of post drug events: (a) confusion matrix: overall accuracy shown in bottom right was 100%, (b) ROC curves. Data files D3 and B3.

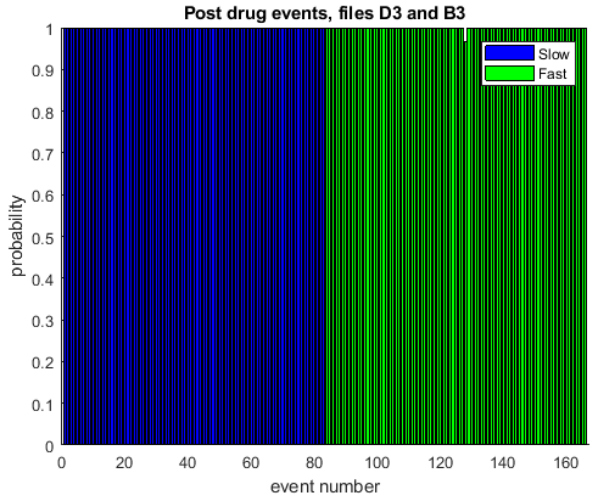

Figure 32: NN classification of post drug events: events 1 to 87 should be blue (slow), events 88 to 174 should be green (fast). Data files D3 and B3.